Decadal coherence of Arctic thermohaline staircases

Mikhail G. Schee[1], **Erica Rosenblum**[1], **Jonathan M. Lilly**[2], **Nicolas Grisouard**[1]

[1]Department of Physics, University of Toronto, Toronto, ON, Canada
[2]Planetary Science Institute, Tucson, AZ, USA

Key Points:

- We detect 48 thermohaline staircase layers across the Beaufort Gyre Region that have nearly constant salinity during 2005–2022.
- The temperature gradient across the staircase weakened by approximately 30% over 17 years, with warm layers cooling and cool layers warming.
- The total height of detected layers compressed by approximately 21.92 dbar in 17 years, with upper layers sinking faster than lower layers.

Corresponding author: Mikhail Schee, `mikhail.schee@alumni.utoronto.ca`

Abstract

Thermohaline staircase layers have been consistently observed in the Arctic Ocean for over 50 years. Previous studies demonstrate that these structures exhibit large-scale spatial coherence. However, on time scales beyond a few years, both the coherence and evolution of the layers are unknown. Using Ice-Tethered Profiler data from 2005–2022 in the Beaufort Gyre Region, we track staircase layers across time and space with an unsupervised clustering method. Individual layers are found to be coherent across the entire 17-year time period, with properties that appear to evolve on 40–50 year timescales or longer. This establishes, for the first time, the decadal-scale coherence of thermohaline staircases in the Arctic Ocean. Moreover, we find that the observed changes are not consistent with the staircase being in a state of equilibrium, but rather support the hypothesis that it is decaying slowly from an initial or on-going perturbation.

Plain Language Summary

In the Canada Basin of the Arctic Ocean, there is a stack of thin layers that stretch horizontally for hundreds of kilometers, called the thermohaline staircase, where each layer or “step” has a distinct temperature and salinity. This structure affects the vertical transport of heat and nutrients between the deep warm waters from the Atlantic Ocean and the cold surface waters above. Staircase layers have been observed in this region for over 50 years and their large-scale spatial extent has been confirmed at particular points in time. Using machine learning and data from under-ice instruments, we analyze the evolution of individual layers across 17 years. We find that dozens of layers are present across the entire time period and that their properties evolve very slowly, establishing the very long lifetimes of these structures. Further, we find that the total height of the layers is compressing and that temperature changes vertically across the staircase are becoming smaller, both of which impact vertical heat transport. These layers are being influenced by the rapidly changing Arctic, and this raises the question as to whether they will continue to exist in the future.

1 Introduction

The Arctic Ocean is projected to warm at a rate of up to three times that of the global ocean average by 2100, part of the phenomenon known as Arctic Amplification (Shu et al., 2022). The largest contribution to this warming is expected to come from Atlantic Water (AW). Occupying depths between 250 and 800 m, this water mass forms the most significant heat reservoir in the Arctic Ocean (Richards et al., 2022) and has already warmed markedly since the mid-twentieth century (Carmack et al., 1997; Polyakov, Pnyushkov, & Timokhov, 2012). The strong stratification found in the thermocline separates the colder surface waters from the heat in the AW (Aagaard et al., 1981; Timmermans et al., 2008), and is important in mediating vertical transport of heat and nutrients (Carmack, 2007; Bluhm et al., 2015; Randelhoff et al., 2020).

In the Canada Basin of the Arctic Ocean, and particularly in the Beaufort Gyre Region (BGR), the thermocline exhibits a characteristic structure called a thermohaline staircase: A series of homogeneous layers, each on the order of meters thick, separated by sharp gradient interfaces in temperature and salinity. Hydrographic profiles containing staircase layers have been observed many times in the Canada Basin: At Ice Island T-3 (Neshyba et al., 1971), during the Arctic Internal Wave Experiment (AIWEX) (Padman & Dillon, 1987), during the Surface Heat Budget of the Arctic (SHEBA) experiment (Shaw & Stanton, 2014), and from Ice-Tethered Profilers (ITPs), automated instruments moored to ice floes that have been consistently deployed since 2004 (Toole et al., 2011). Owing to their role in vertical heat flux (Ménesguen et al., 2022), it is important to understand the long-term evolution of these staircase layers in order to make accurate predictions about the rapidly changing Arctic.

Timmermans et al. (2008) noted that hydrographic profiles from a wide area where staircases are present tend to exhibit clusters in temperature–salinity space, demonstrating that individual staircase layers can stretch hundreds of kilometers horizontally. Previous studies have tracked specific layers across time spans from less than a week (Neshyba et al., 1972; Padman & Dillon, 1988), to about a year (Polyakov, Pnyushkov, Rembe, et al., 2012; Ménesguen et al., 2022), to Lu et al. (2022), who analyzed thousands of ITP profiles between 2005–2009, tracking 34 distinct layers. Yet, staircase layers have been consistently observed in the Canada Basin for over 50 years, raising the possibility that individual layers could remain coherent on decadal or longer time scales.

Recent studies note a decline in the occurrences of staircase layers in the sections of profiles just above the AW (Ménesguen et al., 2022; Lundberg & Polyakov, 2025) and predict that these layers will become thinner over time (Shibley & Timmermans, 2022). While the exact mechanisms behind this transition are as of yet unclear, it coincides with changes in the large-scale circulation and a decline in sea ice cover, rising temperatures below the staircase in the AW, and a cumulative downwelling of around 2–5 m yr^{-1} in the BGR (Meneghello et al., 2018; Proshutinsky et al., 2019; Timmermans & Toole, 2023). If the staircase layers in this region are coherent over long timescales, it would be expected that they would be impacted by these large scale changes.

While many studies have used the wealth of ITP data to analyze Arctic thermohaline staircase layers (Timmermans et al., 2008; Shibley et al., 2017; Shibley & Timmermans, 2019; van der Boog et al., 2021; Lundberg & Polyakov, 2025), their detection methods treat profiles individually, and therefore do not automatically track individual layers over time. Schee et al. (2024) presented an algorithm that automatically detects and connects staircase layers across many different profiles. Here, we apply this algorithm to 17 years of BGR profiles in order to analyze the structure and evolution of staircase layers. In Section 2, we describe our methods to process the data and connect the layers across time. We present our results in Section 3, examining of the coherence of the detected layers and their temporal evolution. Implications of these results are discussed in Section 4.

2 Methods

2.1 Observations

We use an ITP data product that consists of vertical profiles of practical salinity, potential temperature, and pressure at ∼25 cm resolution (Krishfield et al., 2008), which we convert to absolute salinity S_A and conservative temperature Θ (Text S1). The profiler travels up and down a wire attached to the surface buoy roughly two to three times daily and has a salinity precision of ±0.005 g kg^{-1} and a temperature precision of ±0.001°C (Toole et al., 2011). We use only the ascending profiles because descending profiles sample the wake of the unit itself, as the instruments are located at the top of the profiler. Figure 1a shows a typical ITP temperature and salinity profile with thermohaline staircase layers.

In this study we focus on the BGR, which we define as 130–160°W and 73–81.5°N (Figure 1b), following Shibley and Timmermans (2022). We select only profiles within the BGR, and define our date range to start on August 15, 2005—when the almost-continuous ITP coverage of the BGR began—and to end on the same date in 2022. This results in 23,876 profiles, which we refer to as *All BGR* data, the temperature–salinity (Θ–S_A) histogram of which is shown in Figure 1c. A distinct pattern is evident, with dozens of regions with high concentrations of observations that line along near-constant lines of salinity. This is evidence of staircase layers (Timmermans et al., 2008; Bebieva & Timmermans, 2019), as measurements are more likely to fall within mixed layers where temperature and salinity are fairly constant as opposed to within the thin interfaces.

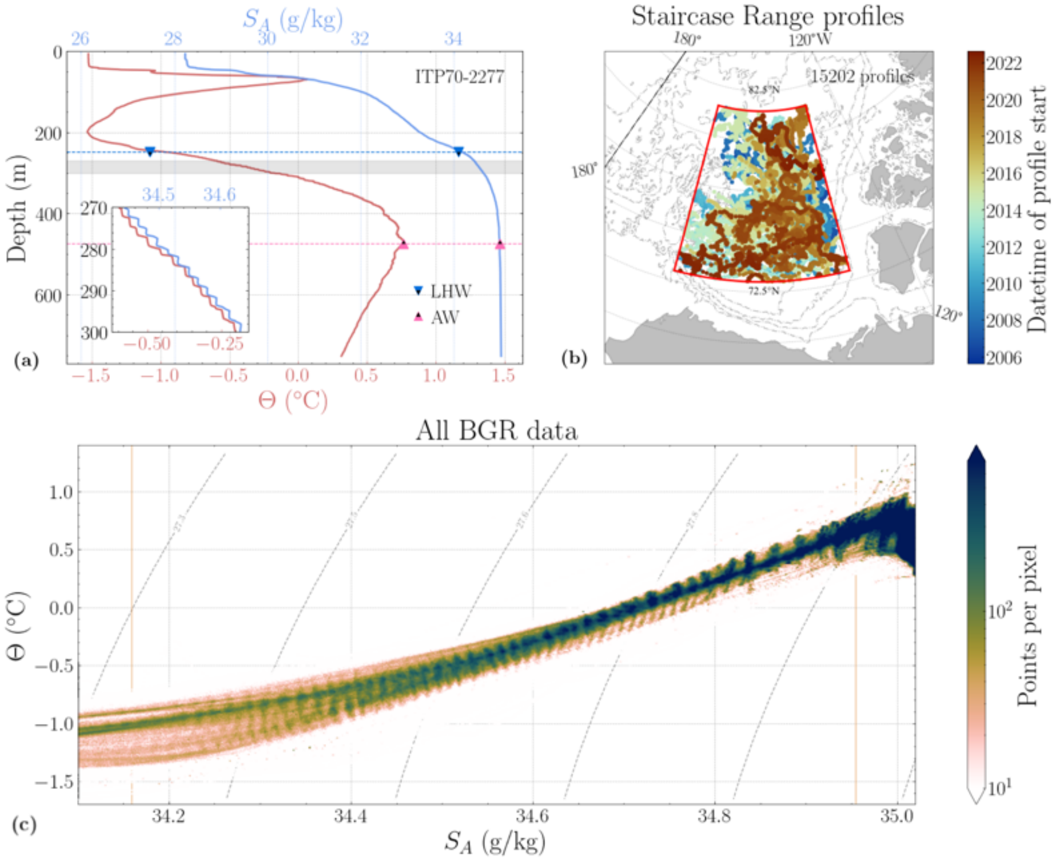

Figure 1. (a) An illustrative ITP temperature and salinity profile, ITP70-2277, taken on 12 March 2014 at 74.6°N, 150.0°W, with the cores of the LHW and AW water masses noted. The highlighted depth range corresponds to the depth range of the inset figure, chosen to show staircase layers. (b) A map of the BGR showing the locations and observation times of *Staircase Range* profiles, with dashed lines showing bathymetric contours. (c) A histogram of observations in temperature–salinity space for *All BGR* data with lines of constant potential density anomaly referenced to the surface. Orange vertical lines denote the salinity range of the *Connected Layers* dataset.

Next, we exclude profiles that do not extend past 400 dbar to ensure they reach the known depth range of the staircase, similar to Shibley and Timmermans (2022), resulting in 15,202 profiles (Figure 1b). Across much of the BGR, a dense spatial coverage with samples in a range of different years is observed. Finally, we focus on the vertical section where staircases features are known to occur, selecting only the observations located between the core of the lower halocline waters (LHW) and the core of the AW (Figure 1a). Similar to Lu et al. (2022) and Shibley and Timmermans (2022), we define the LHW core to be the pressure level at which S_A is closest to 34.1 g kg^{-1}, and the AW core to be the temperature maximum where pressure is greater than 100 dbar to avoid erroneous surface measurements (Shibley et al., 2017). This results in 12,744,846 data points which we refer to as the *Staircase Range* data.

2.2 Clustering and Connecting Layers

We sort the *Staircase Range* data into layers in two steps: Applying the Hierarchical Density-Based Spatial Clustering of Applications with Noise (HDBSCAN) algorithm (Campello et al., 2013) in temperature–salinity space, then dividing the data into layers based on the local minima in the histogram of their salinity. While either method by itself would result in an estimate of staircase layers, we apply both in sequence for a conservative dataset containing the most likely layer observations. The clustering method does not distinguish between individual profiles and may cluster points from different profiles together regardless of how far apart in time or space they were taken. To avoid making the implicit assumption that layers could remain coherent for longer, we split the data into 17 consecutive year-long periods, each starting and ending on August 15, chosen because new ITPs are annually deployed around that date (Figure S1).

First, we apply HDBSCAN in the manner presented by Schee et al. (2024), with minor modifications (Text S2), to each year-long period. We find the clusters align well with the regions of high observation density noted in Figure 1c. On average, each period has 66 clusters with a standard deviation of 11 (Table S1). We note that differences in the number of clusters per year is primarily attributed to those detected within the lower portion of the staircase, $S_A > 34.93$; these will largely be disregarded in the process of connecting layers across periods. We refer to the set of observations that includes all cluster points from all year-long periods as the *Clustered* dataset. Our implementation of HDBSCAN is conservative, favoring missing points which are likely within layers rather than including false positives. Therefore, there are significantly fewer *Clustered* data than *Staircase Range* data.

Second, we examine the local minima in the histograms of salinity shown in Figure 2a–d. The peaks and troughs correspond to the pattern of the Θ–S_A histogram (Figure 1c) and are evident in both the *Staircase Range* and *Clustered* data. We find the local minima to define boundaries between layers, similar to Lu et al. (2022), by first taking a moving average of the *Clustered* data histogram using a window width of 0.1 g kg^{-1}, which is 10 times larger than the average span in salinity for all clusters. The boundaries are then the minima of the salinity histogram that lie between adjacent intersections with its moving average, marked by vertical lines in Figure 2a–d. We find 49 such boundaries and define 48 layers to be the sets of *Clustered* data which lie between each pair of boundaries regardless of the year in which they occur. We refer to this result as the *Connected Layers* dataset. This reduces the salinity range to between the outermost boundaries, 34.159–34.955 g kg^{-1}, marked by orange vertical lines in Figure 2. Within this restricted range, the number of clusters per year-long period in the *Clustered* data is an average of 55 with a standard deviation of 7.

The layers exhibit large-scale spatial variations which would alias into temporal variability on account of spatial differences in year-to-year sampling distributions. Before taking temporal trends, we account for these spatial variations by finding the residual

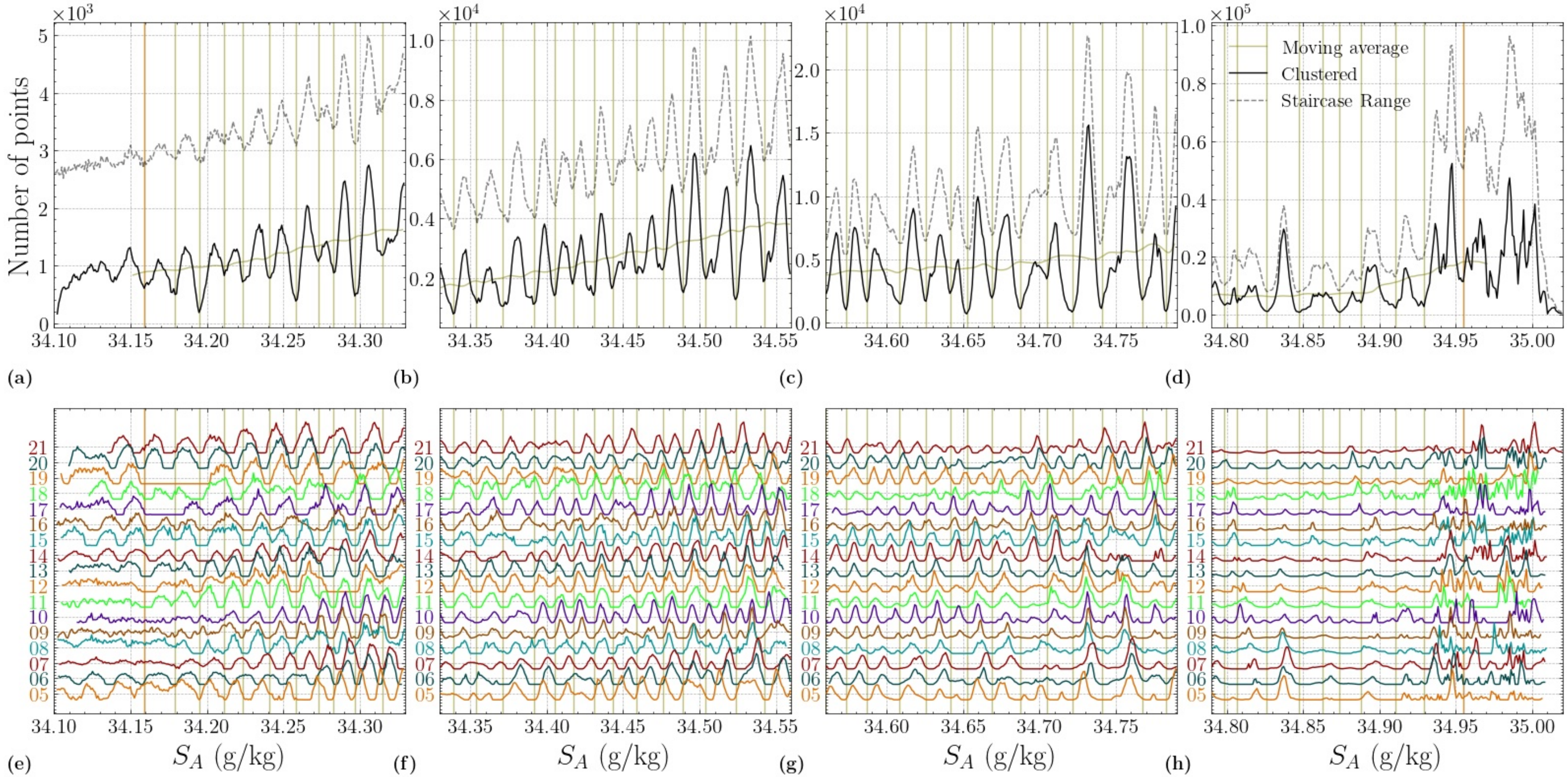

Figure 2. (a–d) Histograms of salinity for *Staircase Range* data (dashed black), *Clustered* data (solid black), and the moving average of the *Clustered* data (yellow) for four different salinity ranges, separated to allow different vertical scales. Solid vertical lines indicate local minima of the *Clustered* data histograms. Orange vertical lines denote the salinity range of the *Connected Layers* dataset. (e–h) Normalized histograms of salinity showing each one-year time period using *Clustered* data, where the different years have been offset vertically. Each time period is labeled by the last two digits of the year in which it began, i.e. 05 is the period from 15 August 2005 to 15 August 2006.

of the data with a two-dimensional polynomial fit of a layer with respect to latitude and longitude (Text S3). In Section 3, we present various lines of evidence to support the claim that these boundaries define coherent layers that span the entire time period, then examine the layer properties and evolution in detail.

3 Results

3.1 Decadal Coherence of Staircase Layers

We begin exploring the coherence of staircase layers by examining the Θ–S_A histogram of *All BGR* data in Figure 1c. The pattern of observations grouping along near-constant lines of salinity is evidence of staircase layers and the same pattern is evident in the peaks and troughs of the salinity histogram in Figure 2a–d when using only the *Clustered* data. In Figure 2e–f, we compute the same histogram for each year separately and find similar results. The peaks are visually trackable from year to year, supporting the conclusion that the layers they represent are coherent across time.

We note that some peaks shift slightly in salinity between years. For example, between periods 14–21 in the salinity range 34.45–34.50 g kg^{-1} (Figure 2f), the peaks shift towards lower salinity values at approximately the same order of magnitude as the salinity precision of the ITPs per year, which is an order of magnitude smaller than the typical distance between peaks. While evidence suggests these shifts are more likely a physical phenomenon than an instrumental drift (Text S4), we do not attempt to account for these drifts in this study as the peaks in the salinity histogram for all years clearly show evidence of staircase layers. In Text S5, we describe an alternate approach of manually connecting layers by subjectively labeling apparently related clusters from year to year. The results are qualitatively the same as those obtained using the method described in Section 2.2, and bolsters the claim that the salinity boundaries we use for the subsequent results define physically meaningful layers.

Figure 3 presents the evolution of the 48 detected staircase layers, with the different layers indicated by different colors. In salinity, the layers are distinct, having well-separated and non-overlapping ranges across time. To quantify this separation, we find the average across all layers of their standard deviations in salinity to be $(3.93\pm0.92)\times 10^{-3}$ g kg^{-1} and note this is an order of magnitude smaller than the average distance between the average values of two neighboring layers, $(1.65\pm0.34)\times10^{-2}$ g kg^{-1} (Table S2). Moreover, there are long-term patterns of evolution in temperature and pressure that regularly cross multiple year-long periods. The occasional discontinuities, which are evident in temperature and pressure yet notably absent in salinity, are likely due to a new deployment of ITPs sampling different regions within the BGR from the previous batch, thus aliasing the spatial variability into temporal variability.

Close inspection of Figure 3 reveals some imperfections in the method. In a couple instances, a detected layer is absent from a particular period, which could be due to gaps in the observations. Notably, there are a few instances where what appears to be two distinct bands of salinity which are grouped into one detected layer, for example, in 2010–2011 between 34.5–34.6 g kg^{-1}. This could due to the physical process of layers merging or splitting over time. The method we use defines layer boundaries across the entire time period and therefore cannot account for such events. The detected layers we present here do not exactly match the underlying staircase structure. They do, however, provide a quantification of what is evident from the histograms above and even in the raw data (Figure S14): There are staircase layers which remain coherent across the 17-year period.

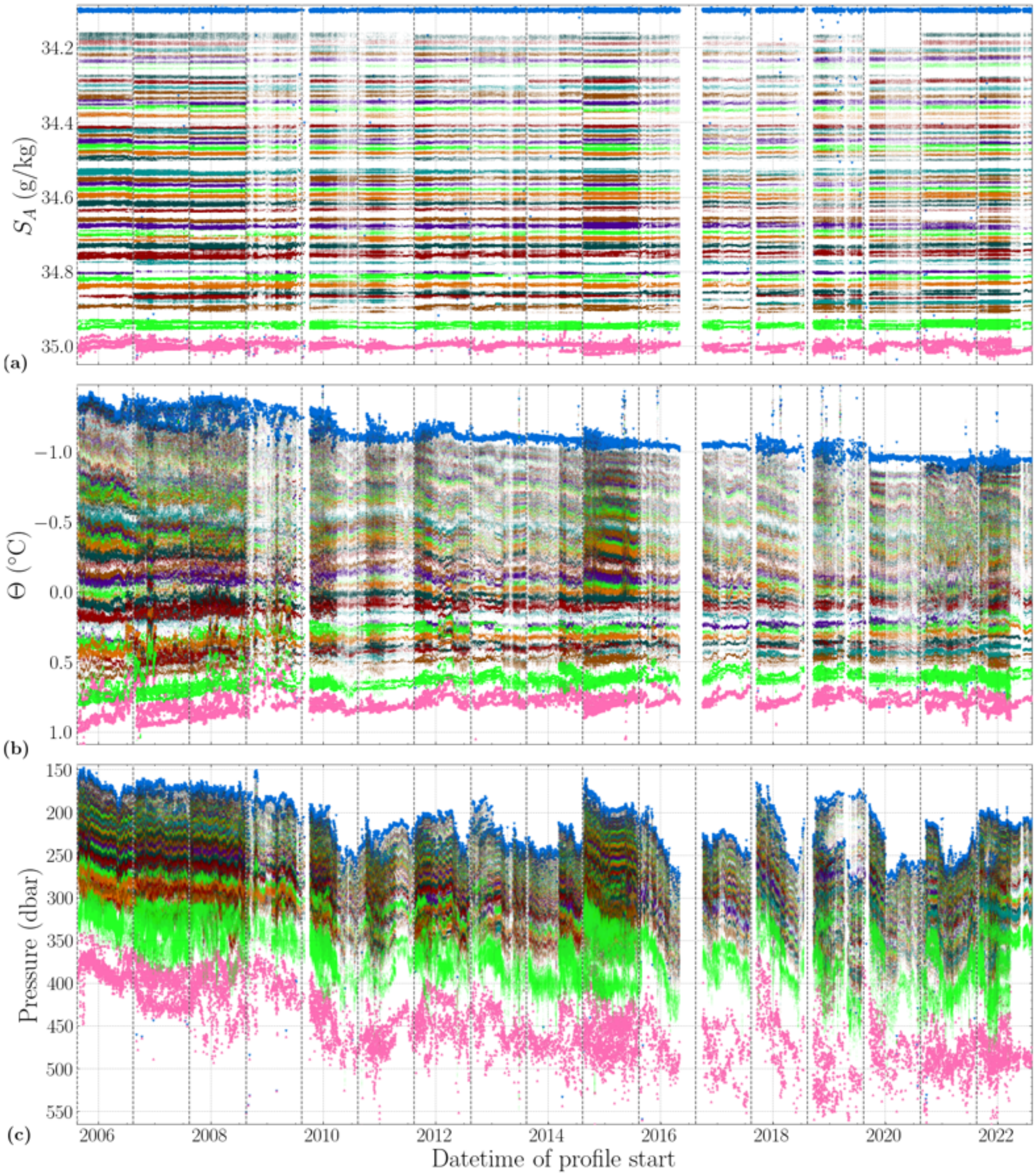

Figure 3. The temporal evolution of (a) salinity, (b) temperature, and (c) pressure of the *Connected Layers* data, where different staircase layers are given different colors. Blue and pink markers denote the values of the LHW and AW, respectively, for each profile. The vertical dashed lines on every August 15th denote the boundary between time periods.

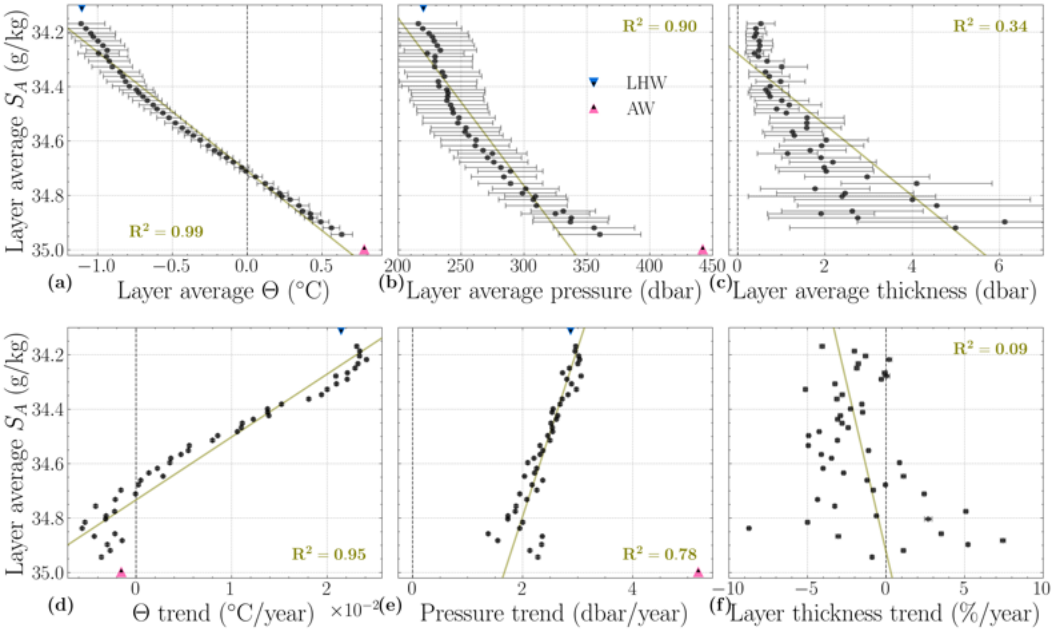

Figure 4. Averages and trends for all detected staircase layers over the entire 17-year period as functions of layer average salinity. The top row shows layer average (a) temperature, (b) pressure, and (c) thickness, with horizontal error bars representing the standard deviation. Vertical error bars represent each layer's standard deviation in salinity, but are too small to be visible. The bottom row shows the trends in (d) temperature, (e) pressure, and (f) thickness after accounting for spatial variations. Layer thickness trends in (f) have been normalized to show percent changes relative to the average thicknesses presented in (c). Linear fits between layer average salinity and each variable are shown in yellow, with their R^2 noted in each panel.

3.2 Staircase Vertical Structure and Evolution

In Figure 4, we present the structure of the staircase temperature, pressure, and thickness as functions of layer average salinity, together with the evolution of that structure. We use layer average salinity, which increases with depth, as a vertical axis as those values remain stable across time. To calculate layer thicknesses, we treat each profile individually and take the difference between the maximum and minimum pressures for each layer. When calculating average layer thicknesses cross all profiles in Figure 4c, we first eliminate all values equal to zero, which occur when a profile has only one point for a particular layer.

For the vertical structure, Figure 4a–c, we find an approximately linear relationship between layer average salinity and temperature, with $R^2 = 0.99$, as well as between layer average salinity and pressure, with $R^2 = 0.90$. Across the entire staircase, we find the median of layer average thicknesses to be 1.28 dbar. While the dependence of layer average thickness on salinity is not as robust as for the other two variables, Figure 4c still implies that layer thickness tends to increase towards higher salinities, from < 0.5 m in the upper water column to $\sim$5 m at depth.

We present the temporal trends in temperature, pressure, and thickness for each detected layer in Figure 4d–f. Each temporal trend for each layer was calculated using a linear fit between the layer's values for a particular variable and time (Figure S6). For temperature, Figure 4d shows a clear pattern across the staircase: Layers near the top have warming trends that decrease with depth and transition to cooling trends near the bottom. A least squares fit gives a robust compound temporal and salinity trend with $R^2 = 0.95$ (Table S3). The salinity level at which temperature trends cross zero is 34.73 g kg^{-1} (approximately 284 dbar), which is very close to the salinity level of 34.71 g kg^{-1} at which the layer average temperature is 0°C (approximately 289 dbar). That is, layers colder than 0°C are warming and layers warmer than 0°C are cooling. This results in the temperature gradient reducing by approximately 30% over the 17-year period from $(1.57 \pm 0.03) \times 10^{-2}$ °C dbar^{-1} in 2005–2006 to $(1.08 \pm 0.02) \times 10^{-2}$ °C dbar^{-1} in 2021–2022.

We find that all values of the trends in pressure for each layer in Figure 4e are positive; all layers are sinking over time, with an average rate of 2.40±0.42 dbar yr^{-1}. The deeper the layer, the slower it is sinking, with the linear fit to this salinity dependency having $R^2 = 0.78$. From this, we calculate that the total height across all detected layers decreased by -21.92 ± 1.76 dbar over 17 years (Text S7). Conversely, the AW core, below the staircase, is sinking at 5.19±0.04 dbar yr^{-1}, notably faster than the bottom-most detected layer at 2.276 ± 0.004 dbar yr^{-1}, implying a widening pressure gap between the two.

This decrease in overall height implies that each detected layer is growing thinner over time. In Figure 4f, we show the trends in layer thickness as percent changes from the layer average thicknesses in 4c in order to facilitate layer comparison across the staircase. This reveals a far more scattered pattern than for the other two variables. While 37 of the 48 layers have negative thickness trends, their R^2 values are, overall, much smaller than those for trends in temperature and pressure (Table S4). We find that 43 of the 48 layers have percent changes in thickness per year between -5% and 5%, with the shallowest 10 layers having an average absolute value of $(7.81 \pm 8.18) \times 10^{-3}$ dbar yr^{-1} and the deepest 10 layers with 0.159±0.126 dbar yr^{-1} (Figure S16). The median absolute trend in thickness is 0.026 dbar yr^{-1} and, over the course of 17 years, the calculated trends in layer thickness for the majority of layers would amount to a change in thickness on the same order of magnitude as the vertical resolution of the measurements, about 0.25 dbar. This, in conjunction with the compression in total height across the layers, implies that they are thinning, but at rates too slow to be sufficiently resolved in this study.

4 Discussion

Using an objective analysis method that allows us to detect and track individual layers over a 17-year time period, this study establishes decadal-scale coherence of Arctic thermohaline staircase layers. This greatly extends previous assessments of their lifetimes, as earlier studies only tracked individual layers for a few years at a time (Polyakov, Pnyushkov, Rembe, et al., 2012; Ménesguen et al., 2022; Lu et al., 2022). Our characterization allows us to form novel estimates of how layer salinity, temperature, pressure, and thickness change over time, resulting in a unique window into the long-term evolution of the Beaufort Gyre's thermohaline staircase.

We find the salinity values of the detected layers are distinct and non-overlapping. The spread within layers is an order of magnitude smaller than the difference between neighboring layers, matching the values reported by Lu et al. (2022). Salinity histograms from individual years (Figure 2e–h) suggest that layers may be freshening at around 0.005 g kg^{-1} yr^{-1}. If this rate represents a physical phenomenon, it would take over 150 years for layer salinity to traverse the entire salinity range we analyze. However, the possibility that this is the result of instrumental drift cannot be ruled out, which could imply layer salinity evolves at still longer timescales. A rigorous treatment of long-term salinity changes which carefully accounts for sensor uncertainties would be a welcome direction for future work.

The Arctic's Atlantic Water layer has been warming over the last half-century (Carmack et al., 1997; Polyakov, Pnyushkov, & Timokhov, 2012), yet we find that lower staircase layers are cooling while upper layers are warming. The net heat flux across the staircase is estimated to be 0.021 W m^{-2} (Text S6), on the same order of magnitude of estimates from previous studies (Timmermans et al., 2008; Turner, 2010; Guthrie et al., 2015). Additionally, we find that the temperature gradient across the staircase reduces by approximately 30% over the 17-year period. If this trend continues, all detected layers would reach a uniform temperature within 40 years.

The detected layers are sinking at 2.40 dbar yr^{-1} on average, consistent with the reported 2–5 m yr^{-1} of cumulative downwelling within the Beaufort Gyre (Meneghello et al., 2018; Proshutinsky et al., 2019). We note that our results were found using *in situ* measurements below sea ice, while previous estimates of downwelling are based on Ekman transport derived from surface stress fields. This agreement implies that the slowly-evolving staircase is passively advected by the gyre-scale vertical velocity field. However, upper layers are sinking faster than lower layers at rates which, if extrapolated, would imply that the total vertical range of the staircase would collapse to zero in approximately 200 years.

We find typical layer thicknesses that match those reported in previous studies (Padman & Dillon, 1987; Lu et al., 2022). Shibley and Timmermans (2022) predicted that layers in the Canada Basin will become thinner over time. While we find that most layer thickness trends are negative, the implied thickness changes over the 17-year record are comparable to the vertical resolution of the measurements for the majority of the layers. Despite these thickness trends being only marginally resolved, it is clear from the overall compression of the staircase that layers must be thinning. If they are indeed thinning at the calculated rates, most of the detected layers would disappear in about 50 years.

The fact that staircase layers appear to remain coherent over this 17-year period raises the possibility that all observations of staircases in the Canada Basin to date describe a single, slowly-evolving staircase of large horizontal scale. Importantly, the rates of change we find in the detected layers' salinity, temperature, pressure, and thickness all imply lifetimes of decades or longer. This seems to preclude a scenario in which the layers observed over the historical record represent distinct features that are repeatedly created and destroyed.

These results are also relevant for the nature of the staircase's long-term evolution. A couple scenarios are plausible: the staircase is in a state of slow spin-down from a perturbation, or it represents an equilibrium configuration in which layers continually form, evolve, and decay. If the staircase is a transient feature, its genesis could have involved a large-scale lock exchange event as speculated by Bebieva and Timmermans (2019), analogous to the laboratory experiments by Ruddick et al. (1999). Alternatively, the staircase could be in an equilibrium state by undergoing constant renewal through a process of layers forming near the AW core and then slowly being conveyed upwards, becoming thinner and fresher. This is in line with the consensus from laboratory, theory, and observations that layer thickness increases with depth (Neal et al., 1969; Padman & Dillon, 1987; Guo et al., 2016; Shibley & Timmermans, 2019), as well as with laboratory experiments that show staircase layers freshening over time (Huppert & Linden, 1979). A combination of these scenarios is also possible, with the staircase initially in equilibrium then perturbed into a transient state.

The results presented here are more consistent with the Beaufort Gyre staircase being currently in a slow spin-down. While we find layer thickness increasing with depth and salinities possibly decreasing over time, in line with the equilibrium hypothesis, we also find that the temperature gradient and total height of all detected layers are decreasing, both of which appear to be inconsistent with a state of equilibrium. The matter is far from closed. Obtaining a better understanding the decadal and longer scale evolution of thermohaline staircases, incorporating observations and well as theory and experiments, would be a promising topic for future work. This is particularly important as the Arctic Ocean is currently undergoing rapid changes that may act as major perturbations to these long-lived structures.

Open Research Section

Replication code can be found on Zenodo: `https://doi.org/10.5281/zenodo.14925731`. The Ice-Tethered Profiler data were collected and made available by the Ice-Tethered Profiler Program (Toole et al., 2011; Krishfield et al., 2008; Toole et al., 2016) based at the Woods Hole Oceanographic Institution (`https://www2.whoi.edu/site/itp/`).

Acknowledgments

M.G.S. and N.G. acknowledge the support of the Natural Sciences and Engineering Research Council of Canada (NSERC) [RGPIN-2022-04560]. E.R. acknowledges support by the NSERC Discovery Grant (funding reference number RGPIN-2024-05545). J.M.L. acknowledges the support of award #2319610 from the Physical Oceanography program of the United States National Science Foundation.

References

Aagaard, K., Coachman, L., & Carmack, E. (1981). On the halocline of the Arctic Ocean. *Deep Sea Research Part A. Oceanographic Research Papers*, *28*(6), 529–545. doi: 10.1016/0198-0149(81)90115-1

Bebieva, Y., & Timmermans, M. L. (2019). Double-Diffusive Layering in the Canada Basin: An Explanation of Along-Layer Temperature and Salinity Gradients. *Journal of Geophysical Research: Oceans*, *124*(1), 723–735. doi: 10.1029/2018JC014368

Bluhm, B., Kosobokova, K., & Carmack, E. (2015). A tale of two basins: An integrated physical and biological perspective of the deep Arctic Ocean. *Progress in Oceanography*, *139*, 89–121. doi: 10.1016/j.pocean.2015.07.011

Campello, R. J. G. B., Moulavi, D., & Sander, J. (2013). Density-Based Clustering Based on Hierarchical Density Estimates. *Lecture Notes in Computer Science*, *7819*, 160–172. doi: 10.1007/978-3-642-37456-2_14

Carmack, E. C. (2007). The alpha/beta ocean distinction: A perspective on freshwater fluxes, convection, nutrients and productivity in high-latitude seas. *Deep-Sea Research Part II: Topical Studies in Oceanography*, *54*(23-26), 2578–2598. doi: 10.1016/j.dsr2.2007.08.018

Carmack, E. C., Aagaard, K., Swift, J. H., Macdonald, R. W., McLaughlin, F. A., Jones, E. P., . . . Killiush, L. R. (1997). Changes in temperature and tracer distributions within the Arctic Ocean: Results from the 1994 Arctic Ocean section. *Deep-Sea Research Part II: Topical Studies in Oceanography*, *44*(8), 1487–1493. doi: 10.1016/S0967-0645(97)00056-8

Guo, S., Zhou, S., Qu, L., & Lu, Y. (2016). Laboratory experiments on diffusive convection layer thickness and its oceanographic implications. *Journal of Geophysical Research: Oceans*, *121*(10), 7517–7529. doi: 10.1002/2016JC012172

Guthrie, J. D., Fer, I., & Morison, J. (2015). Observational validation of the diffusive convection flux laws in the Amundsen Basin, Arctic Ocean. *Journal of Geophysical Research: Oceans*, *120*(12), 7880–7896. doi: 10.1002/2015JC010884

Huppert, H. E., & Linden, P. F. (1979). On heating a stable salinity gradient from below. *Journal of Fluid Mechanics*, *95*(3), 431–464. doi: 10.1017/S0022112079001543

Krishfield, R., Toole, J., & Timmermans, M. (2008). ITP Data Processing Procedures. *Woods Hole Oceanographic Institution*(March), 1–24. Retrieved from `https://www2.whoi.edu/site/itp/wp-content/uploads/sites/92/2019/08/ITP_Data_Processing_Procedures_35803.pdf`

Lu, Y.-Z., Guo, S.-X., Zhou, S.-Q., Song, X.-L., & Huang, P.-Q. (2022). Identification of Thermohaline Sheet and Its Spatial Structure in the Canada Basin. *Journal of Physical Oceanography*, *52*(11), 2773–2787. doi: 10.1175/JPO-D-22-0012.1

Lundberg, M., & Polyakov, I. V. (2025). Climate Change Drives Evolution of Thermohaline Staircases in the Arctic Ocean. *Journal of Geophysical Research: Oceans*, *130*(1), 1–26. doi: 10.1029/2024JC021538

Meneghello, G., Marshall, J., Timmermans, M.-L., & Scott, J. (2018). Observations of Seasonal Upwelling and Downwelling in the Beaufort Sea Mediated by Sea Ice. *Journal of Physical Oceanography*, *48*(4), 795–805. doi: 10.1175/JPO-D-17-0188.1

Ménesguen, C., Lique, C., & Caspar-Cohen, Z. (2022). Density Staircases Are Disappearing in the Canada Basin of the Arctic Ocean. *Journal of Geophysical Research: Oceans*, *127*(11). doi: 10.1029/2022JC018877

Neal, V. T., Neshyba, S., & Denner, W. (1969). Thermal Stratification in the Arctic Ocean. *Science*, *166*(3903), 373–374. doi: 10.1126/science.166.3903.373

Neshyba, S., Neal, V. T., & Denner, W. (1971). Temperature and Conductivity Measurements under Ice Island T-3. *Journal of Geophysical Research*, *76*(33), 8107–8120. doi: 10.1029/JC076i033p08107

Neshyba, S., Neal, V. T., & Denner, W. W. (1972). Spectra of Internal Waves: In-Situ Measurements in a Multiple-Layered Structure. *Journal of Physical Oceanography*, *2*(1), 91–95. doi: 10.1175/1520-0485(1972)002⟨0091:SOIWSM⟩2.0.CO;2

Padman, L., & Dillon, T. M. (1987). Vertical Heat Fluxes Through the Beaufort Sea Thermohaline Staircase. *Journal of Geophysical Research*, *92*(C10), 10799. doi: 10.1029/JC092iC10p10799

Padman, L., & Dillon, T. M. (1988). On the Horizontal Extent of the Canada Basin Thermohaline Steps. *Journal of Physical Oceanography*, *18*(10), 1458–1462. doi: 10.1175/1520-0485(1988)018⟨1458:OTHEOT⟩2.0.CO;2

Polyakov, I. V., Pnyushkov, A. V., Rembe, R., Ivanov, V. V., Lenn, Y. D., Padman, L., & Carmack, E. C. (2012). Mooring-based observations of double-diffusive staircases over the laptev sea slope. *Journal of Physical Oceanography*, *42*(1), 95–109. doi: 10.1175/2011JPO4606.1

Polyakov, I. V., Pnyushkov, A. V., & Timokhov, L. A. (2012). Warming of the Intermediate Atlantic Water of the Arctic Ocean in the 2000s. *Journal of Climate*, *25*(23), 8362–8370. doi: 10.1175/JCLI-D-12-00266.1

Proshutinsky, A., Krishfield, R., Toole, J. M., Timmermans, M. L., Williams, W., Zimmermann, S., . . . Zhao, J. (2019). Analysis of the Beaufort Gyre Freshwater Content in 2003–2018. *Journal of Geophysical Research: Oceans*, *124*(12), 9658–9689. doi: 10.1029/2019JC015281

Randelhoff, A., Holding, J., Janout, M., Sejr, M. K., Babin, M., Tremblay, J. É., & Alkire, M. B. (2020). Pan-Arctic Ocean Primary Production Constrained by Turbulent Nitrate Fluxes. *Frontiers in Marine Science*, *7*(March), 1–15. doi: 10.3389/fmars.2020.00150

Richards, A. E., Johnson, H. L., & Lique, C. (2022). Spatial and Temporal Variability of Atlantic Water in the Arctic From 40 Years of Observations. *Journal of Geophysical Research: Oceans*, *127*(9). doi: 10.1029/2021JC018358

Ruddick, B. R., Phillips, O. M., & Turner, J. (1999). A laboratory and quantitative model of finite-amplitude thermohaline intrusions. *Dynamics of Atmospheres and Oceans*, *30*(2-4), 71–99. doi: 10.1016/S0377-0265(99)00021-4

Schee, M. G., Rosenblum, E., Lilly, J. M., & Grisouard, N. (2024). Unsupervised clustering identifies thermohaline staircases in the Canada Basin of the Arctic

Ocean. *Environmental Data Science*, *3*, e13. doi: 10.1017/eds.2024.13

Shaw, W. J., & Stanton, T. P. (2014). Vertical diffusivity of the Western Arctic Ocean halocline. *Journal of Geophysical Research: Oceans*, *119*(8), 5017–5038. doi: 10.1002/2013JC009598

Shibley, N. C., & Timmermans, M. (2022). The Beaufort Gyre's Diffusive Staircase: Finescale Signatures of Gyre-Scale Transport. *Geophysical Research Letters*, *49*(13). doi: 10.1029/2022GL098621

Shibley, N. C., & Timmermans, M.-L. (2019). The Formation of Double-Diffusive Layers in a Weakly Turbulent Environment. *Journal of Geophysical Research: Oceans*. doi: 10.1029/2018JC014625

Shibley, N. C., Timmermans, M.-L., Carpenter, J. R., & Toole, J. M. (2017). Spatial variability of the Arctic Ocean's double-diffusive staircase. *Journal of Geophysical Research: Oceans*, *122*(2), 980–994. doi: 10.1002/2016JC012419

Shu, Q., Wang, Q., Årthun, M., Wang, S., Song, Z., Zhang, M., & Qiao, F. (2022). Arctic Ocean Amplification in a warming climate in CMIP6 models. *Science Advances*, *8*(30), 1–10. doi: 10.1126/sciadv.abn9755

Timmermans, M.-L., Toole, J., Krishfield, R., & Winsor, P. (2008). Ice-Tethered Profiler observations of the double-diffusive staircase in the Canada Basin thermocline. *Journal of Geophysical Research*, *113*, 1–10. doi: 10.1029/2008jc004829

Timmermans, M.-L., & Toole, J. M. (2023). The Arctic Ocean's Beaufort Gyre. *Annual Review of Marine Science*, *15*(1), 223–248. doi: 10.1146/annurev-marine-032122-012034

Toole, J. M., Krishfield, R. A., O'Brien, J. K., & Cole, S. T. (2016). *Ice-Tethered Profiler observations: Vertical profiles of temperature, salinity, oxygen, and ocean velocity from an Ice-Tethered buoy system.* NOAA National Centers for Environmental Information. doi: 10.7289/v5mw2f7x

Toole, J. M., Krishfield, R. A., Timmermans, M. L., & Proshutinsky, A. (2011). The Ice-Tethered profiler: Argo of the Arctic. *Oceanography*, *24*(3), 126–135. doi: 10.5670/oceanog.2011.64

Turner, J. S. (2010). The Melting of Ice in the Arctic Ocean: The Influence of Double-Diffusive Transport of Heat from Below. *Journal of Physical Oceanography*, *40*(1), 249–256. doi: 10.1175/2009JPO4279.1

van der Boog, C. G., Otto Koetsier, J., Dijkstra, H. A., Pietrzak, J. D., & Katsman, C. A. (2021). Global dataset of thermohaline staircases obtained from Argo floats and Ice-Tethered Profilers. *Earth System Science Data*, *13*(1), 43–61. doi: 10.5194/essd-13-43-2021

References From the Supporting Information

IOC. (2010). *The international thermodynamic equation of seawater – 2010 : Calculation and use of thermodynamic properties* (Vol. 56). UNESCO.

Kelley, D. E. (1990). Fluxes through diffusive staircases: A new formulation. *Journal of Geophysical Research*, *95*(C3), 3365. doi: 10.1029/jc095ic03p03365

McDougall, T. J., & Barker, P. M. (2011). *Getting started with TEOS-10 and the Gibbs Seawater (GSW) Oceanographic Toolbox* (3.06.12 ed.). Retrieved from `www.TEOS-10.org`

Millero, F. J. (2010). History of the equation of state of seawater. *Oceanography*, *23*(3), 18–33. doi: 10.5670/oceanog.2010.21

Moulavi, D., Jaskowiak, P. A., Campello, R. J. G. B., Zimek, A., & Sander, J. (2014). Density-Based Clustering Validation. In *Proceedings of the 2014 siam international conference on data mining* (Vol. 2, pp. 839–847). Philadelphia, PA: Society for Industrial and Applied Mathematics. doi: 10.1137/1.9781611973440.96

Oka, E. (2005). Long-term sensor drift found in recovered Argo profiling floats. *Journal of Oceanography*, *61*(4), 775–781. doi: 10.1007/s10872-005-0083-6

Polyakov, I. V., Walsh, J. E., & Kwok, R. (2012). Recent changes of Arctic multiyear sea ice coverage and the likely causes. *Bulletin of the American Meteorological Society*, *93*(2), 145–151. doi: 10.1175/BAMS-D-11-00070.1

Radko, T. (2013). *Double-Diffusive Convection*. Cambridge University Press. doi: 10.1017/CBO9781139034173

Stranne, C., Mayer, L., Weber, T. C., Ruddick, B. R., Jakobsson, M., Jerram, K., … Gårdfeldt, K. (2017). Acoustic Mapping of Thermohaline Staircases in the Arctic Ocean. *Scientific Reports*, *7*(1), 15192. doi: 10.1038/s41598-017-15486-3

GEOPHYSICAL RESEARCH LETTERS

Supporting Information for “Decadal coherence of Arctic thermohaline staircases”

M.G. Schee[1], E. Rosenblum[1], J.M. Lilly[2], N. Grisouard[1]

[1]Department of Physics, University of Toronto, Toronto, ON, Canada

[2]Planetary Science Institute, Tucson, AZ, USA

Contents of this file

1. Text S1 to S7
2. Figures S1 to S17
3. Tables S1 to S3

Additional Supporting Information (Files uploaded separately)

1. Captions for large Table S4

Corresponding author: M.G. Schee, Department of Physics, University of Toronto, McLennan Physical Laboratories, Toronto, ON M5S 3J1, CAN. (mikhail.schee@alumni.utoronto.ca)

Introduction In the Supporting Information, we present additional text, figures, and tables to provide supporting details for the methods used and the results in the main text.

Text S1. Ice-Tethered Profiler Data

The data we use for this study come from the Ice-Tethered Profilers (ITPs) and are archived at the NOAA National Centers for Environmental Information repository (Toole et al., 2016) (accessed September 21, 2023). In order to take full advantage of the ∼25 cm resolution, we follow Timmermans, Toole, Krishfield, and Winsor (2008) and use the Level III Matlab-format data files as opposed to the Level III “final” format which bin-averages the data to a 1-dbar vertical resolution (Krishfield et al., 2008). These profiles have been processed to remove corrupted data, then adjusted for sensor lags which may otherwise round the sharp edges of individual layers, calibrated in salinity on a profile-by-profile basis using the staircase layers themselves as reference, and manually cleaned of any remaining spurious values. The dates at which the profiles used in this study were taken by each ITP are shown in Figure S1 and the Beaufort Gyre Region (BGR) is shown in Figure S2.

In this work, we use the quantity called conservative temperature Θ, the temperature measure recommended by TEOS-10, as opposed to potential temperature θ (McDougall & Barker, 2011). For the range of temperatures and salinities of data analyzed here, the difference $|\theta - \Theta|$ is a systematic shift that is always less than 0.05°C (McDougall & Barker, 2011). We also choose to use absolute salinity S_A, defined as the mass fraction of dissolved non-H_2O material in seawater and is reported in g kg^{-1} (Millero, 2010; IOC, 2010), as opposed to practical salinity S_P, a scale based on the measured conductivity of seawater. While S_P is easier to measure, different samples with the same conductivity from different areas around the ocean can have different compositions, and so conversions are made from S_P to S_A based upon the location of the measurement. We make the conversions to Θ and S_A from the values reported by the ITPs using the implementation of TEOS-10 in the Gibbs Seawater (GSW) Oceanographic Toolbox Python package, version 3.4.0 (McDougall & Barker, 2011).

Text S2. Modifications to the Clustering Method

The method presented by Schee, Rosenblum, Lilly, and Grisouard (2024) involves applying the Hierarchical Density-Based Spatial Clustering of Applications with Noise (HDBSCAN) algorithm (Campello et al., 2013) to staircase data in the parameter space of local temperature anomaly vs. salinity. We apply the same method to each of the 17 year-long periods with two minor modifications.

The first is in calculating the local temperature anomaly, which Schee et al. (2024) define as

$$\Theta'(z) = \Theta(z) - \frac{1}{\ell}\int_{z-\ell/2}^{z+\ell/2} \Theta(z')dz' \tag{1}$$

where $\Theta(z)$ represents an original profile as a function of pressure and ℓ represents the width in dbar of a rectangular moving average window. This was done to more tightly correlate the clusters in Θ'–S_A space than they are in Θ–S_A space. While Schee et al. (2024) used $\ell = 25$ dbar, we use $\ell = 2.5$ dbar as this tightens further the correlation in Θ'–S_A space (see Figure S.4 in the Supplementary Materials for Schee et al. (2024)) and gives more consistent results across different time periods. While Schee et al. (2024) note that a larger ℓ can reveal features such as intrusions near the bottom of the staircase, this study is not focused on such features.

The second difference is in the selection of the single hyperparameter used by HDBSCAN: m_{pts}, the minimum number of points per cluster which is also known as the minimum density threshold. Similar to Schee et al. (2024), we ran the HDBSCAN algorithm 50 times with values of m_{pts} from 50 to 2500 for each time period. Examples of such parameter sweeps for periods 14 and 15 are shown in Figure S3a and S3c with the selected values of m_{pts} circled in red. We see the same general trend in number of clusters as did Schee et al. (2024), rapidly decreasing for small values of m_{pts} then decreasing much more slowly as m_{pts} grows larger.

Our main criteria for selecting an appropriate value of m_{pts} for each period was, following Schee et al. (2024), looking for values which maximize the Density-Based Clustering Validation (DBCV) scores (Moulavi et al., 2014), as long as it does not occur below the values at which the number of clusters is rapidly decreasing. For period 14, this led our selection of $m_{\mathrm{pts}} = 1050$ where DBCV was maximum at 0.2537; this particular clustering is shown in Figure S3b. However, for several periods, this approach led to clusters which aligned poorly with staircase layers. In these cases, we chose a value of m_{pts} that was lower than that with the maximum DBCV, yet a prominent value of DBCV with respect to nearby m_{pts}, using the fact that the optimal value of m_{pts} is roughly proportional to the number of data points. For example, the maximum DBCV of the parameter sweep for period 15 in Figure S3c was 0.1857 at $m_{\mathrm{pts}} = 2150$. However, we chose to use $m_{\mathrm{pts}} = 500$ which gave a prominent value DBCV of 0.1772 compared to nearby points and was at a similar order of magnitude in m_{pts} compared to other periods with a similar order of magnitude number of data points. The chosen clustering for BGR1516 is shown in Figure S3d. Table S1 summarizes the information and parameters used, including values of m_{pts}, for each year-long period. Noise points are those observations which were determined to be noise by HDBSCAN, that is, points which are included in the *Staircase Range* data but not the *Clustered* data.

Text S3. Accounting for Spatial Variability in Layers

We determine the layers' spatial distributions in order to remove the bias from the calculation of their temporal trends which results from the varying spatial sampling of the BGR from year to year. For each of the 48 layers in the *Connected Layers* dataset, we find a bowl-shaped geographic distribution in pressure with the center of the layer being approximately 100 dbar deeper than the edges (see Figure S4), similar to that noted by Lu, Guo, Zhou, Song, and Huang (2022). Over the time period we analyze in this study, the BGR exhibits a cumulative downwelling of around 2–5 m yr^{-1} (Meneghello et al., 2018; Proshutinsky et al., 2019; Timmermans & Toole, 2023). Because this trend in time is orders of magnitude smaller than the differences observed across space, we first account for the horizontal spatial variations, implicitly assuming these variations do not change substantially over the time period.

We do not account for spatial variations in layer thickness as those values are found by taking the difference between maximum and minimum pressure values for a layer. Additionally, as salinity is the variable with which we define the layer boundaries, we do not find its temporal trends, nor do we see any large-scale spatial variations in salinity for any layer. We do, however, note large-scale spatial variations in temperature, and so we account for these variations before calculating temperature trends. We note that these variations change between layers from the top to the bottom of the staircase (see Figure S5) and attribute this, as Lu et al. (2022) did, to the differing temperature influences of the LHW above and the AW below.

To account for large-scale variations, we fit a two-dimensional polynomial over latitude and longitude for a given variable v (i.e., p, or Θ) using the least squares function from the linear algebra module of the Numpy Python library. In order to capture the large-scale features of the spatial distributions while remaining relatively simple, we determine the 10 coefficients, A–J, up to third power in latitude (ϕ) and longitude (λ), from the polynomial model

$$v_{\text{fit}} = A + B\lambda + C\lambda^2 + D\lambda^3 + E\phi + F\lambda\phi + G\lambda^2\phi + H\phi^2 + I\lambda\phi^2 + J\phi^3 \tag{2}$$

for each layer. Example fits of pressure and temperature for several layers are shown in Figure S4 and S5, where they are seen to capture well the overall spatial features. For each layer, and for both temperature and pressure, we next form residuals by subtracting the corresponding spatial fit, $v_{\text{res}}(\phi, \lambda) = v(\phi, \lambda) - v_{\text{fit}}(\phi, \lambda)$. When calculating temporal trends in temperature or pressure for a particular layer, we take a least squares linear regression between the residuals and time using the Stats module from the Scipy Python library. In Figure S6, we show an example of such a temporal trend in pressure for layer 35 where, after taking the residual, the pressure variations drop considerably. The standard errors for these fits either decrease or remain the same after removing the spatial variability, see Table S4. Additionally, the R^2 value of the fit increases after removing spatial variability.

Both points verify that this step allows the temporal trends to be captured with more fidelity.

Text S4. Changes in Salinity Over Time

In Figure 2e–f, we plot salinity histograms for each year separately using the *Clustered* dataset. Generally speaking, patterns of peaks and troughs can be visually tracked from year to year. However, some peaks appear to shift to lower values of salinity across time, for example between 2014–2021 in the salinity range of 34.45–34.50 g kg^{-1}, shown in Figure 2f. Notably, the same shift toward lower salinities is visible in at least a half-dozen different layers and in a succession of years.

It is unclear whether this shift towards lower salinities indicates that layers are actually becoming fresher, or is the result of instrumental drift. The shift in salinity values between years is the same order of magnitude as the salinity precision of the ITPs, around 0.005 g kg^{-1} (Shibley et al., 2017; Bebieva & Timmermans, 2019), and an order of magnitude smaller than the average difference in average salinity between neighboring layers, 0.016 g kg^{-1}. While the long-term salinity changes seen here are comparable in magnitude to instrumental drift (Oka, 2005), in order to account for such drift, ITP salinities are already calibrated on a per-profile basis under the assumption that salinities on deep isotherms remain stable over the deployment period (Krishfield et al., 2008). Moreover, the freshening trend is seen to be contiguous over time periods that correspond to different serial number instruments (see Figure S1). These factors would appear to suggest that the origin of this trend is physical as opposed to instrumental. The distinction is, however, immaterial to the present study, because, in either case, it appears clear that the same layers are being observed across different years.

Despite small year-to-year shifts in salinity, the minima in the yearly histograms—representing the thin gradient regions between well-mixed layers—frequently, but not always, occur in the vicinity of minima of the histogram of the entire 17-year dataset. This fact supports the use of the local minima in Figure 2e–h as a simple definition of the layer boundaries across all years.

Text S5. Manual Layer Connection Method

We find our overall results do not qualitatively change when using a manual approach to connect layers, rather than creating layer boundaries based on a salinity histogram. To illustrate the need to connect layers across time periods, we first plot in Figure S7 the salinity data across all time periods from running HDBSCAN on each year-long period separately. The cluster IDs (and corresponding colors) have been assigned in order of salinity. Schee et al. (2024) noted that the clustering algorithm can sometimes erroneously group multiple layers into a single cluster or erroneously divide one layer into multiple clusters. Therefore, there is no guarantee that staircase layers (correctly-identified or not) will be assigned the same cluster ID for each of the 17 year-long periods and indeed, as seen in Figure S7, the cluster IDs clearly do not line up between time periods.

In our manual approach to connecting clusters into layers across time periods, we label all points within a particular cluster to be within a particular layer, compared to the approach in the main text which sometimes split data points in the same cluster across multiple layers. In this manual labeling process, we follow several guiding principles.

When a cluster in a particular period clearly encompassed more than one layer, we gave that cluster it's own distinct ID if the majority of other periods did, in fact, distinguish those layers. We avoided relabeling two clusters within the same period to the same layer ID unless it was abundantly clear that the clustering algorithm divided one layer into multiple clusters. For values of S_A above approximately 34.9, the number of clusters increased and their spans in S_A decreased, often overlapping with each other. This part of the staircase is very near the AW core, a region known to have intrusions (Bebieva & Timmermans, 2019). Because we are not analyzing intrusions in this study, we did not make an attempt to connect across time periods for clusters with an average $S_A \gtrsim 34.9$ g kg^{-1}, simply assigning them IDs with values of 120 or larger. The result of this manual relabeling can be seen in Figure S8.

Using these manually-connected layers, we create the same plot as Figure 4 in the main text in Figure S9. Note that this includes clusters marked as outliers in both R_L (blue) and IR_{S_A} (red) (see Text S5), as well as having all layers with IDs $\geq$ 120 marked as outliers in both as such layers were not connected across time periods and should not be included in statistics. Using this method, we find the same overall trends, however the standard deviations or standard errors are larger and the R^2 values of the compound trends are smaller. This is mostly due to the layers in this method which only occupy one or two year-long periods. The fact that we find the same trends using two different methods of layer connection across periods shows that these trends are robust.

Text S5. Outlier Clusters in R_L and IR

In this study, we do not disregard outlier layers as Schee et al. (2024) did. In their study, they eliminated outliers in both normalized inter-cluster range IR of salinity and lateral density ratio R_L. IR is defined for a cluster i to be

$$IR_v^i = \frac{v_{max}^i - v_{min}^i}{\min(|\bar{v}^i - \bar{v}^{i-1}|, |\bar{v}^i - \bar{v}^{i+1}|)}, \tag{3}$$

where $i-1$ and $i+1$ are the clusters on either side of i, v is the variable of interest (in this case, S_A), v_{max}^i and v_{min}^i are the maximum and minimum values of v within cluster i, and $\bar{v}^i$ is the cluster's mean value of v.

R_L is defined to be

$$R_L = \frac{\beta \Delta S_A}{\alpha \Delta \Theta}, \tag{4}$$

where the haline contraction and thermal expansion coefficients are $\beta = \rho^{-1}\partial\rho/\partial S_A$, and $\alpha = -\rho^{-1}\partial\rho/\partial\Theta$ respectively, and ΔS_A and $\Delta\Theta$ are, respectively, the variations in salinity and temperature in a particular layer (Radko, 2013; Bebieva & Timmermans, 2019). Here, R_L is estimated by the inverse slope of a linear fit of a particular layer's data in $\alpha\Theta$–βS_A space.

Figure S10 shows the values of IR_{S_A} and R_L for each layer as a function of S_A. The values of IR_{S_A} in this study are all very close to 1 due to how clusters were divided into layers across the year-long periods using a salinity histogram; they necessarily have non-overlapping salinity ranges. As opposed to Schee et al. (2024), we do not find a robust pattern in R_L in relation to pressure. We find no outliers in IR_{S_A} and five outliers in R_L. In Figure S11, we make the same plot as in Figure 4, but show the trends calculated when the outliers are excluded. We note that the trends are very similar to those in Figure 4, and conclude that the inclusion or exclusion of outliers does not affect our overall results.

Text S6. Heat Flux

Estimates of heat flux through thermohaline staircases have often used parametrizations that depend on the jumps in temperature and salinity between neighboring layers (Kelley, 1990; Shibley et al., 2017; Lu et al., 2022) and making direct measurements of heat flux in this part of the ocean is difficult (Polyakov et al., 2012; Stranne et al., 2017). However, estimates of heat flux could be calculated from long-term temperature trends of staircase layers.

Previous studies have estimated this using parameterizations, such as the 4/3 flux law, based upon the differences in temperature and salinity between adjacent layers (Kelley, 1990; Shibley et al., 2017; Lu et al., 2022). Using layer temperature trends $\overline{\mathrm{d}_t\Theta}$, average thickness $\overline{\Delta h}$, isobaric heat capacity $\overline{C_p}$, and density $\overline{\rho}$, we calculate the net heat flux $\overline{\Delta\mathcal{F}_H}$ for each layer as

$$\overline{\Delta\mathcal{F}_H} = \overline{\Delta h}\cdot\overline{C_p}\cdot\overline{\mathrm{d}_t\Theta}\cdot\overline{\rho} \tag{5}$$

and plot them in Figure S12. We find there is an internal structure within the staircase which matches the trends in temperature with upper layers warming and lower layers cooling. 44 of 48 layers have net heat fluxes between -0.003 and 0.002 W/m^2. While these calculations do not indicate the physical direction of the heat flux, the sum of layers' net heat fluxes, after removing one outlier (layer 48), is 0.021 W/m^2 which is the same order of magnitude of estimates from previous studies (Timmermans et al., 2008; Turner, 2010;

Guthrie et al., 2015; Shibley & Timmermans, 2019) and is only a small fraction of the estimates of total ocean-to-sea-ice heat flux (Timmermans et al., 2008).

Text S7. Calculating Timescales of Layer Evolution

In this section, we present the calculations of various values related to the timescales of layer evolution presented in the main text.

From the salinity histograms of individual years in Figure 2e–h, we estimate that certain peaks may be shifting in salinity at approximately 0.005 g kg^{-1} yr^{-1}. The outer salinity boundaries of the *Connected Layers* dataset are 34.159–34.955 g kg^{-1}, spanning 0.796 g kg^{-1}. Therefore, we estimate that it would take approximately 0.796 g kg^{-1}/0.005 g kg^{-1} yr^{-1} = 159 years for a peak to cross that entire salinity range.

We find the temperature gradient across the detected layers to be decreasing over time. In 2005–2006, the temperature gradient as a function of pressure was $(1.57 \pm 0.03) \times 10^{-2}$ °C dbar^{-1}. In 2021–2022, it was $(1.08 \pm 0.02) \times 10^{-2}$ °C dbar^{-1}. This gives a $100 \times (1 - 1.08/1.57) = 31.2\%$ decrease. This calculation holds for the temperature gradient as a function of salinity as well. In 2005–2006, it was 2.77 ± 0.03 °C (g kg^{-1})$^{-1}$ and in 2021-2022, it was 1.93 ± 0.05 °C (g kg^{-1})$^{-1}$. This gives a $100 \times (1 - 1.93/2.77) = 30.3\%$ decrease.

In Figure 4e, the average of the layer's trends in pressure is 2.40 dbar yr^{-1} with a standard deviation of 0.42 dbar yr^{-1}. Shallower layers are sinking faster than deeper layers, with a compound temporal and salinity trend of -1.62 ± 0.13 dbar yr^{-1} (g kg^{-1})$^{-1}$ with $R^2 = 0.78$. We use this to calculate the decrease in total height of the staircase by extrapolating the boundaries of the analyzed salinity range

$$[-1.62 \text{ dbar yr}^{-1}(\text{g kg}^{-1})^{-1} \times 17 \text{ yr}](34.955 \text{ g kg}^{-1} - 34.159 \text{ g kg}^{-1}) = -21.92 \text{ dbar}$$

with the uncertainty range propagated by extrapolating with the compound trend's upper

$$[(-1.62{+}0.13) \text{ dbar yr}^{-1}(\text{g kg}^{-1})^{-1}{\times}17 \text{ yr}](34.955 \text{ g kg}^{-1}{-}34.159 \text{ g kg}^{-1}) = -23.681 \text{ dbar}$$

and lower bound

$$[(-1.62{-}0.13) \text{ dbar yr}^{-1}(\text{g kg}^{-1})^{-1}{\times}17 \text{ yr}](34.955 \text{ g kg}^{-1}{-}34.159 \text{ g kg}^{-1}) = -20.16 \text{ dbar}$$

resulting in a calculated compression of -21.92 ± 1.76 dbar.

This value takes into account the significant spatial variations in pressure exhibited by the layers (see Figure S4). Because of these fluctuations, the difference in pressure between the top and bottom detected layers at various points in time should not be taken as an accurate estimate of change in overall staircase height. However, it may be useful to use differences between the top and bottom layers to estimate the average height of the staircase, which can then give context to the estimated 21.92 dbar compression. In Figure S17, we show the layer average pressure of the top and bottom layers, as well as the difference between those two. From this, we estimate an average total height of the layers of the staircase across all year-long periods to be 137 dbar. From this, compression of 21.92 dbar then represents approximately a 16% decrease.

To estimate a timescale for this evolution in the pressure of layers, we take the trends, which account for spatial variability, of the top and bottom layers, and solve for when they intersect. The top layer is changing in pressure by

$$p_{bottom}(t) = 215.91 \text{ dbar} + 2.96 \text{ dbar yr}^{-1}(t)$$

and, for the bottom

$$p_{bottom}(t) = 360.28 \text{ dbar} + 2.276 \text{ dbar yr}^{-1}(t)$$

Solving for their intersection

$$215.91 \text{ dbar} + 2.96 \text{ dbar yr}^{-1}(t) = 360.28 \text{ dbar} + 2.276 \text{ dbar yr}^{-1}(t)$$
$$0.684 \text{ dbar yr}^{-1}(t) = 144.37 \text{ dbar}$$
$$t = 211 \text{ yr}$$

We note that this compression is only for the layers we detect. There may be layers or other similar features present that were not detected that would contribute to the overall height of the staircase. For example, the bottom-most detected layer is sinking at 2.276 ± 0.004 dbar yr^{-1} while the AW core is sinking at 5.19 ± 0.04 dbar yr^{-1}, implying that these two features are diverging away from each other in pressure. The gap between these two comes from the connection method used in the study. While the AW core reached salinities of up to 35.02 g kg^{-1}, the bottom-most layer's salinity boundary is 34.955 g kg^{-1}. This part of the water column is known to contain features called intrusions, which are thought to run down to form staircase layers (Bebieva & Timmermans, 2019).

For the layer thickness trends, we find a median percent change of -1.94% for all the detected layers. Extrapolating this would mean that the thickness of most layers would collapse to zero in on the order of 50 years. We note, however, that the magnitudes of these changes are on the same order as the vertical resolution of the measurements, ~ 0.25 dbar. As we calculate the layer thickness on a profile-by-profile basis, the values of thickness are generally centered around multiples of 0.25 dbar (see Figure S16a). To obtain higher-precision estimates of these small layerwise thickness trends, future work could consider longer time series, incorporate data from other contemporary sources such as ship casts or mooring, or estimate layer thickness using multiple profiles.

References

Bebieva, Y., & Timmermans, M. L. (2019). Double-Diffusive Layering in the Canada Basin: An Explanation of Along-Layer Temperature and Salinity Gradients. *Journal of Geophysical Research: Oceans*, *124*(1), 723–735. doi: 10.1029/2018JC014368

Campello, R. J. G. B., Moulavi, D., & Sander, J. (2013). Density-Based Clustering Based on Hierarchical Density Estimates. *Lecture Notes in Computer Science*, *7819*, 160–172. doi: 10.1007/978-3-642-37456-2_14

Guthrie, J. D., Fer, I., & Morison, J. (2015). Observational validation of the diffusive convection flux laws in the Amundsen Basin, Arctic Ocean. *Journal of Geophysical Research: Oceans*, *120*(12), 7880–7896. doi: 10.1002/2015JC010884

IOC. (2010). *The international thermodynamic equation of seawater – 2010 : Calculation and use of thermodynamic properties* (Vol. 56). UNESCO.

Kelley, D. E. (1990). Fluxes through diffusive staircases: A new formulation. *Journal of Geophysical Research*, *95*(C3), 3365. doi: 10.1029/jc095ic03p03365

Krishfield, R., Toole, J., & Timmermans, M. (2008). ITP Data Processing Procedures. *Woods Hole Oceanographic Institution*(March), 1–24. Retrieved from `https://www2.whoi.edu/site/itp/wp-content/uploads/sites/92/2019/08/ITP_Data_Processing_Procedures_35803.pdf`

Lu, Y.-Z., Guo, S.-X., Zhou, S.-Q., Song, X.-L., & Huang, P.-Q. (2022). Identification of Thermohaline Sheet and Its Spatial Structure in the Canada Basin. *Journal of*

Physical Oceanography, *52*(11), 2773–2787. doi: 10.1175/JPO-D-22-0012.1

McDougall, T. J., & Barker, P. M. (2011). *Getting started with TEOS-10 and the Gibbs Seawater (GSW) Oceanographic Toolbox* (3.06.12 ed.). Retrieved from `www.TEOS-10.org`

Meneghello, G., Marshall, J., Timmermans, M.-L., & Scott, J. (2018). Observations of Seasonal Upwelling and Downwelling in the Beaufort Sea Mediated by Sea Ice. *Journal of Physical Oceanography*, *48*(4), 795–805. doi: 10.1175/JPO-D-17-0188.1

Millero, F. J. (2010). History of the equation of state of seawater. *Oceanography*, *23*(3), 18–33. doi: 10.5670/oceanog.2010.21

Moulavi, D., Jaskowiak, P. A., Campello, R. J. G. B., Zimek, A., & Sander, J. (2014). Density-Based Clustering Validation. In *Proceedings of the 2014 siam international conference on data mining* (Vol. 2, pp. 839–847). Philadelphia, PA: Society for Industrial and Applied Mathematics. doi: 10.1137/1.9781611973440.96

Oka, E. (2005). Long-term sensor drift found in recovered Argo profiling floats. *Journal of Oceanography*, *61*(4), 775–781. doi: 10.1007/s10872-005-0083-6

Polyakov, I. V., Walsh, J. E., & Kwok, R. (2012). Recent changes of Arctic multiyear sea ice coverage and the likely causes. *Bulletin of the American Meteorological Society*, *93*(2), 145–151. doi: 10.1175/BAMS-D-11-00070.1

Proshutinsky, A., Krishfield, R., Toole, J. M., Timmermans, M. L., Williams, W., Zimmermann, S., . . . Zhao, J. (2019). Analysis of the Beaufort Gyre Freshwater Content in 2003–2018. *Journal of Geophysical Research: Oceans*, *124*(12), 9658–9689. doi: 10.1029/2019JC015281

Radko, T. (2013). *Double-Diffusive Convection.* Cambridge University Press. doi: 10.1017/CBO9781139034173

Schee, M. G., Rosenblum, E., Lilly, J. M., & Grisouard, N. (2024). Unsupervised clustering identifies thermohaline staircases in the Canada Basin of the Arctic Ocean. *Environmental Data Science*, *3*, e13. doi: 10.1017/eds.2024.13

Shibley, N. C., & Timmermans, M. (2022). The Beaufort Gyre's Diffusive Staircase: Finescale Signatures of Gyre-Scale Transport. *Geophysical Research Letters*, *49*(13). doi: 10.1029/2022GL098621

Shibley, N. C., & Timmermans, M.-L. (2019). The Formation of Double-Diffusive Layers in a Weakly Turbulent Environment. *Journal of Geophysical Research: Oceans*. doi: 10.1029/2018JC014625

Shibley, N. C., Timmermans, M.-L., Carpenter, J. R., & Toole, J. M. (2017). Spatial variability of the Arctic Ocean's double-diffusive staircase. *Journal of Geophysical Research: Oceans*, *122*(2), 980–994. doi: 10.1002/2016JC012419

Stranne, C., Mayer, L., Weber, T. C., Ruddick, B. R., Jakobsson, M., Jerram, K., … Gårdfeldt, K. (2017). Acoustic Mapping of Thermohaline Staircases in the Arctic Ocean. *Scientific Reports*, *7*(1), 15192. doi: 10.1038/s41598-017-15486-3

Timmermans, M.-L., Toole, J., Krishfield, R., & Winsor, P. (2008). Ice-Tethered Profiler observations of the double-diffusive staircase in the Canada Basin thermocline. *Journal of Geophysical Research*, *113*, 1–10. doi: 10.1029/2008jc004829

Timmermans, M.-L., & Toole, J. M. (2023). The Arctic Ocean's Beaufort Gyre. *Annual Review of Marine Science*, *15*(1), 223–248. doi: 10.1146/annurev-marine-032122

-012034

Toole, J. M., Krishfield, R. A., O'Brien, J. K., & Cole, S. T. (2016). *Ice-Tethered Profiler observations: Vertical profiles of temperature, salinity, oxygen, and ocean velocity from an Ice-Tethered buoy system.* NOAA National Centers for Environmental Information. doi: 10.7289/v5mw2f7x

Turner, J. S. (2010). The Melting of Ice in the Arctic Ocean: The Influence of Double-Diffusive Transport of Heat from Below. *Journal of Physical Oceanography*, *40*(1), 249–256. doi: 10.1175/2009JPO4279.1

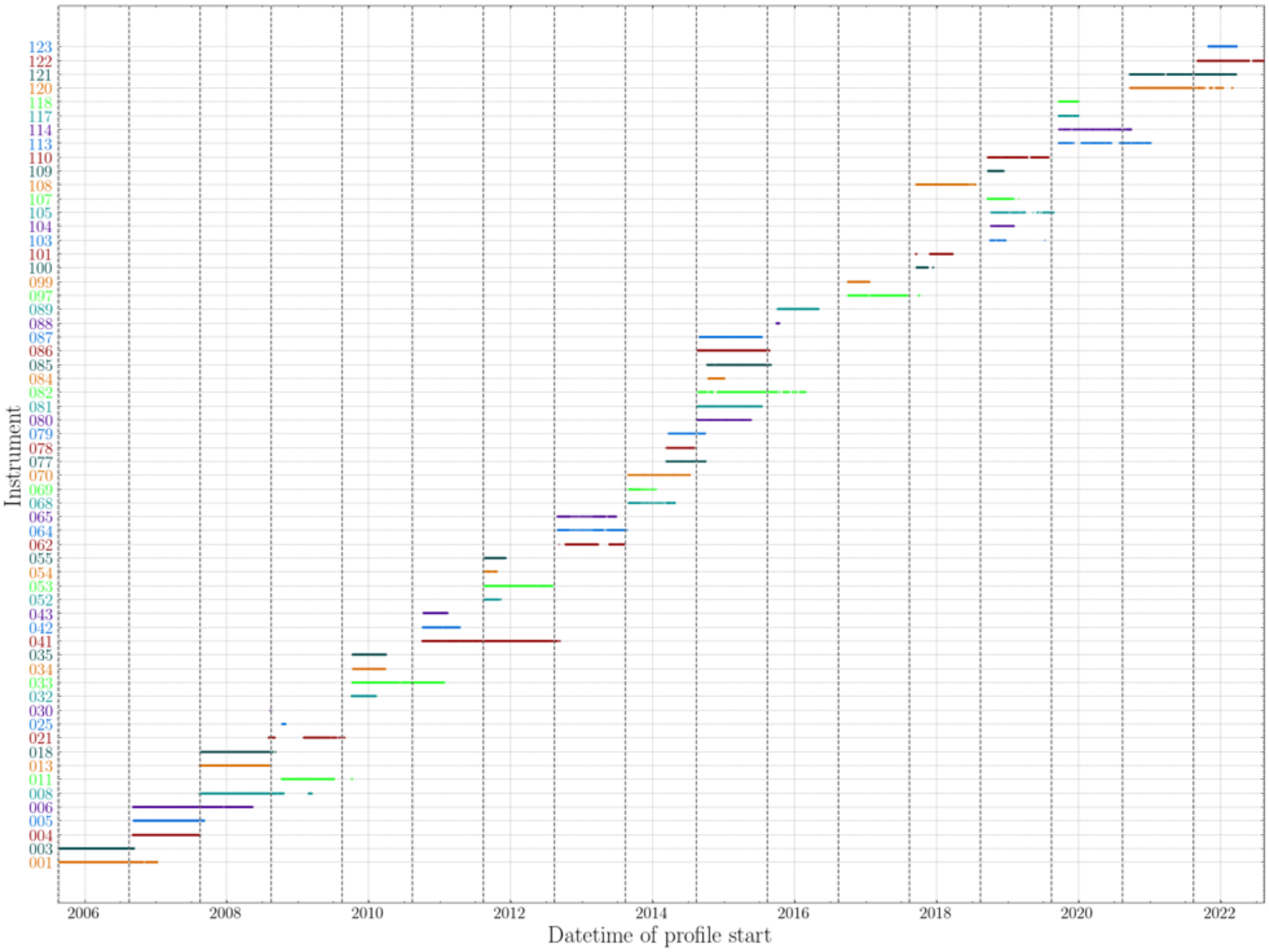

Figure S1. The dates on which profiles were taken within the BGR (see Figure S2) with respect to it's instrument ID in the time period analyzed in this study. This shows only the 15,202 up-going profiles which extend past 400 dbar (*Staircase Range* data). The vertical dashed lines indicate the 15th of August in each year, around when new ITPs have typically been deployed. Note that the colors for each ITP are only to make them easier to distinguish and do not correspond to certain clusters or layers with the same color in other plots.

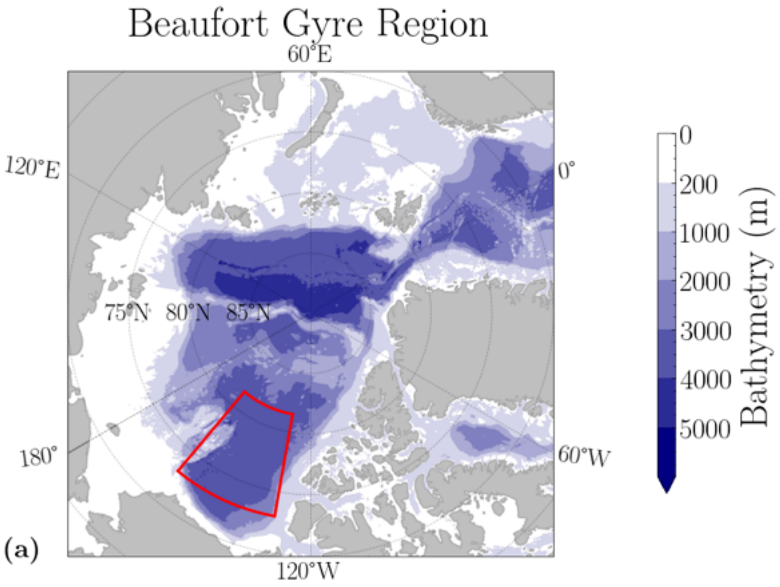

Figure S2. A map of the Arctic with the Beaufort Gyre Region (BGR) boxed in red. Following Shibley and Timmermans (2022), we define the BGR boundaries to be 130–160°W and 73–81.5°N.

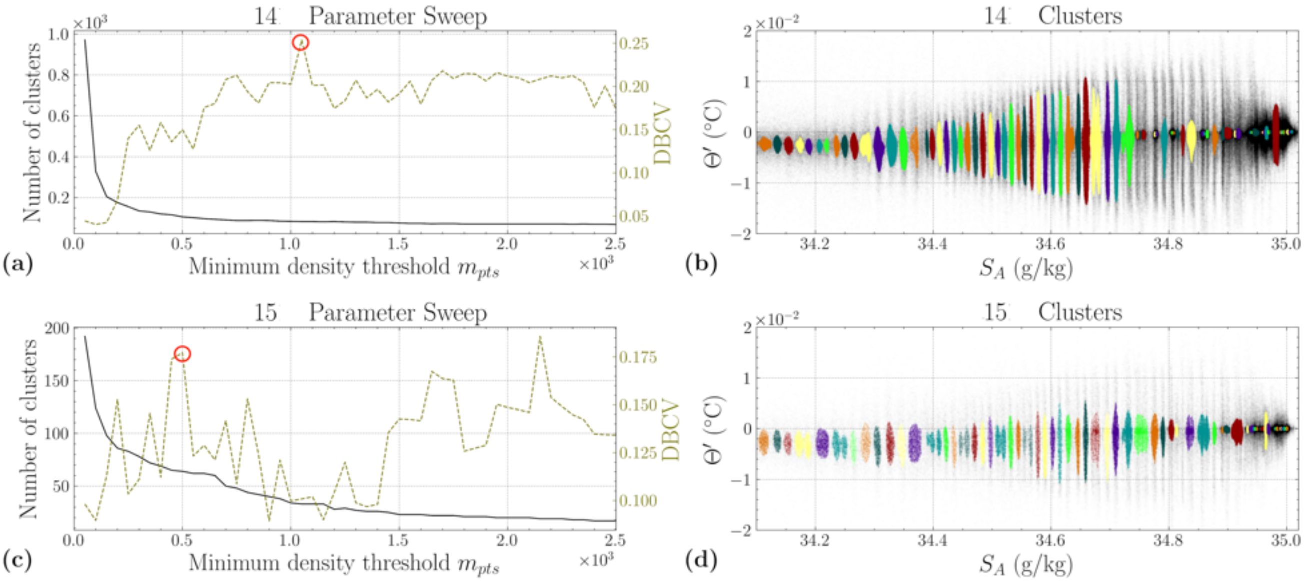

Figure S3. Parameter sweeps in m_{pts} for periods (a) 14 and (c) 15. The results of clustering periods (b) 14 and (d) 15 with the chosen values of m_{pts} 1050 and 500, respectively, before dividing layers based upon the salinity histogram.

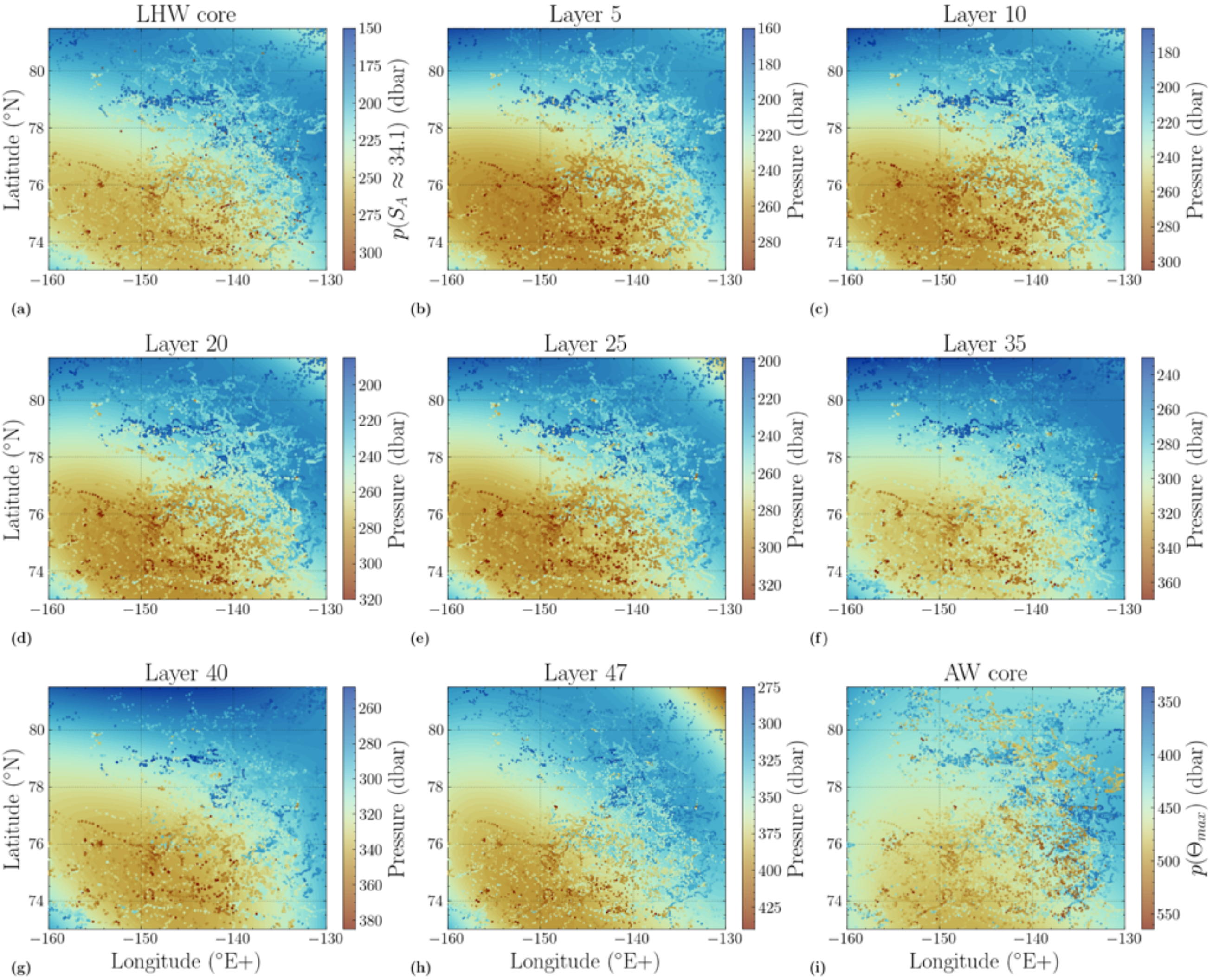

Figure S4. Maps of the pressure of each point within a layer over contour plots of the fit of that layer for the LHW core, a selection of layers, as well as the AW core. The layers are in order of physically highest to lowest in the water column.

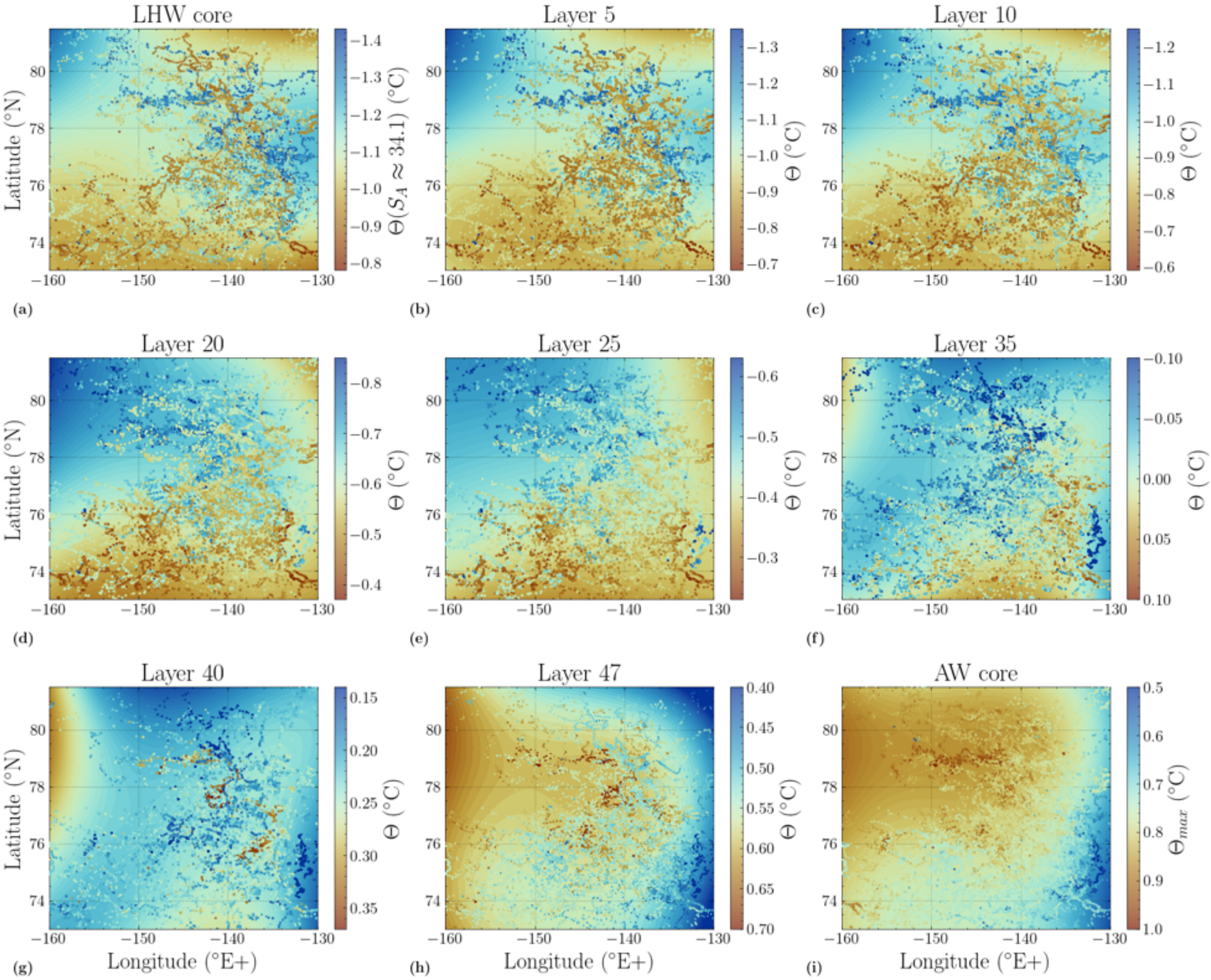

Figure S5. Maps of the temperature of each point within a layer over contour plots of the fit of that layer for the LHW core, a selection of layers, as well as the AW core. The layers are in order of physically highest to lowest in the water column.

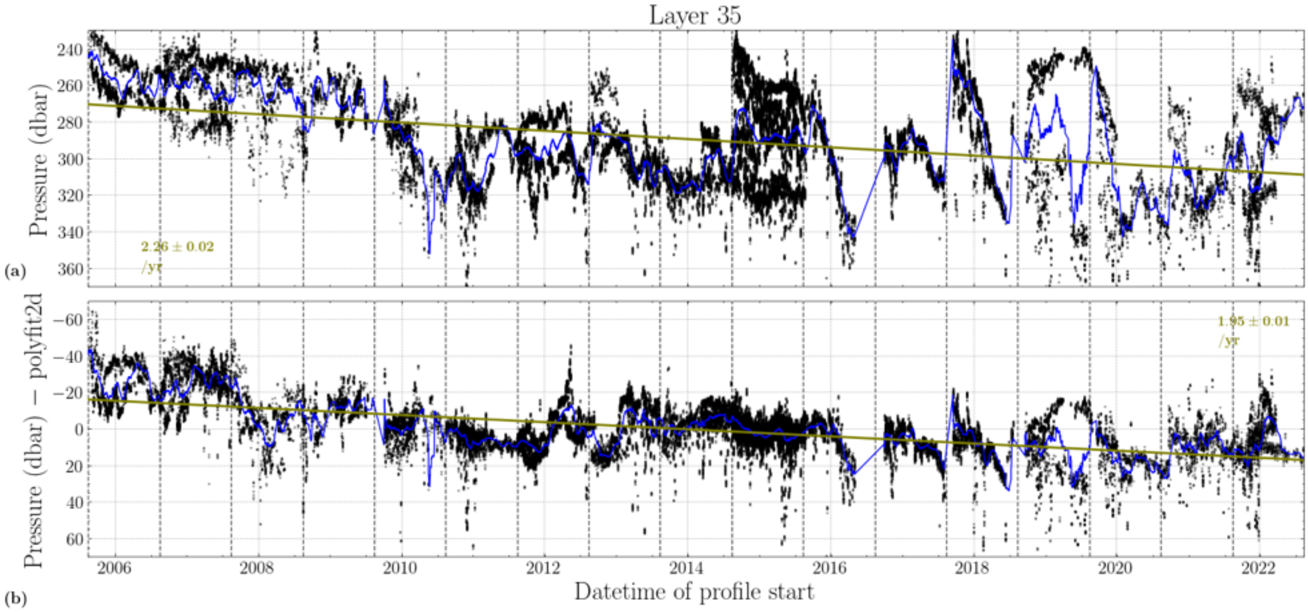

Figure S6. An example for the pressures in detected layer 35 of the least-squares linear fit used to determine trends in time. (a) The linear fit for the data before accounting for spatial variations. (b) The linear fit for the data after having accounted for spatial variations, and the slope of pressure change over time used for layer 35 in the study.

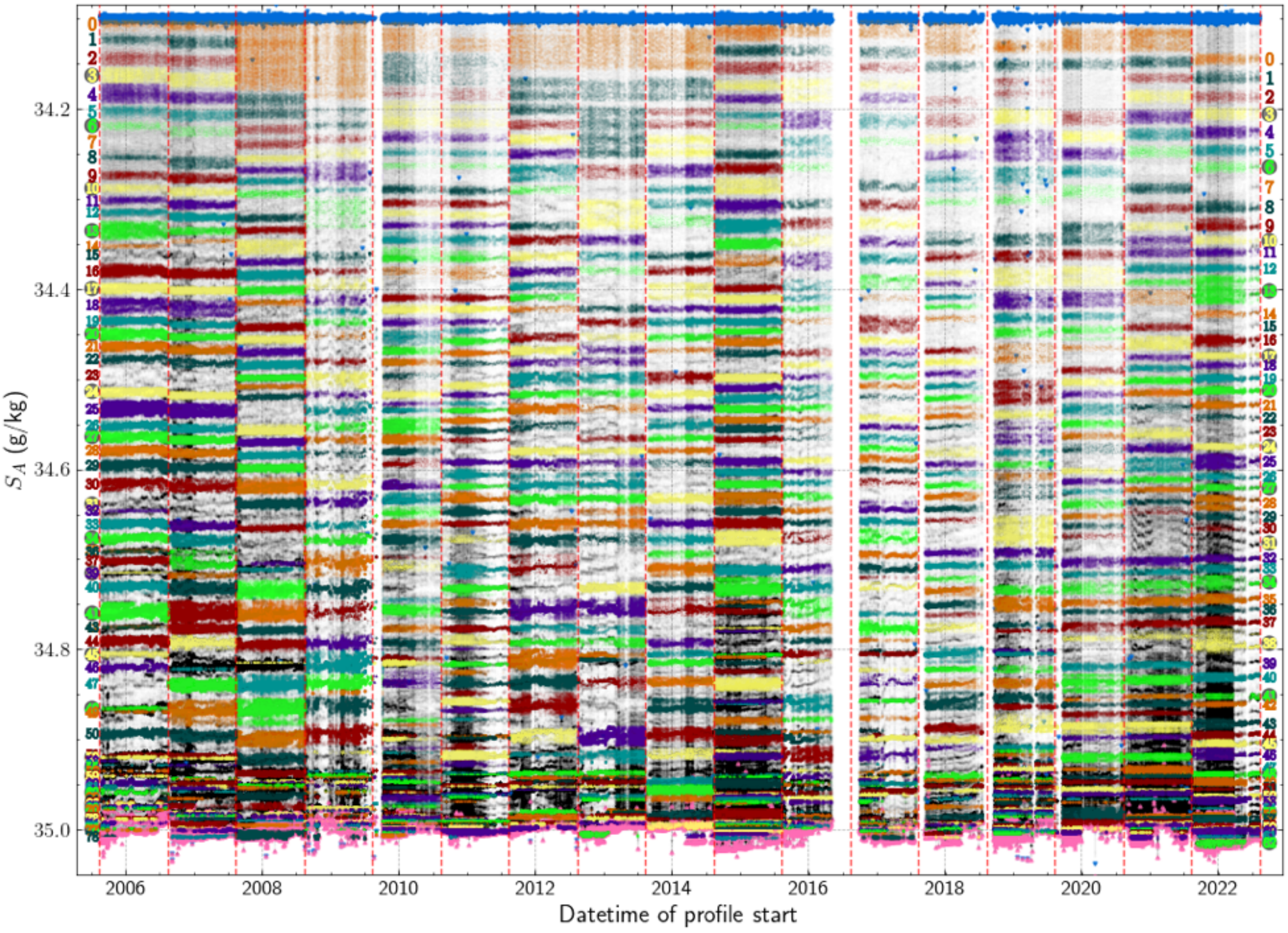

Figure S7. The salinity across all time periods, colored by cluster, before connecting layers across time periods. Noise points are marked in black. The blue and pink triangle markers denote the values of the LHW and AW, respectively, for each profile. The vertical dashed lines appear on every August 15th to denote the boundary between time periods. The IDs for clusters in period 05 (21) are shown by the colored numbers on the left (right) of the plot.

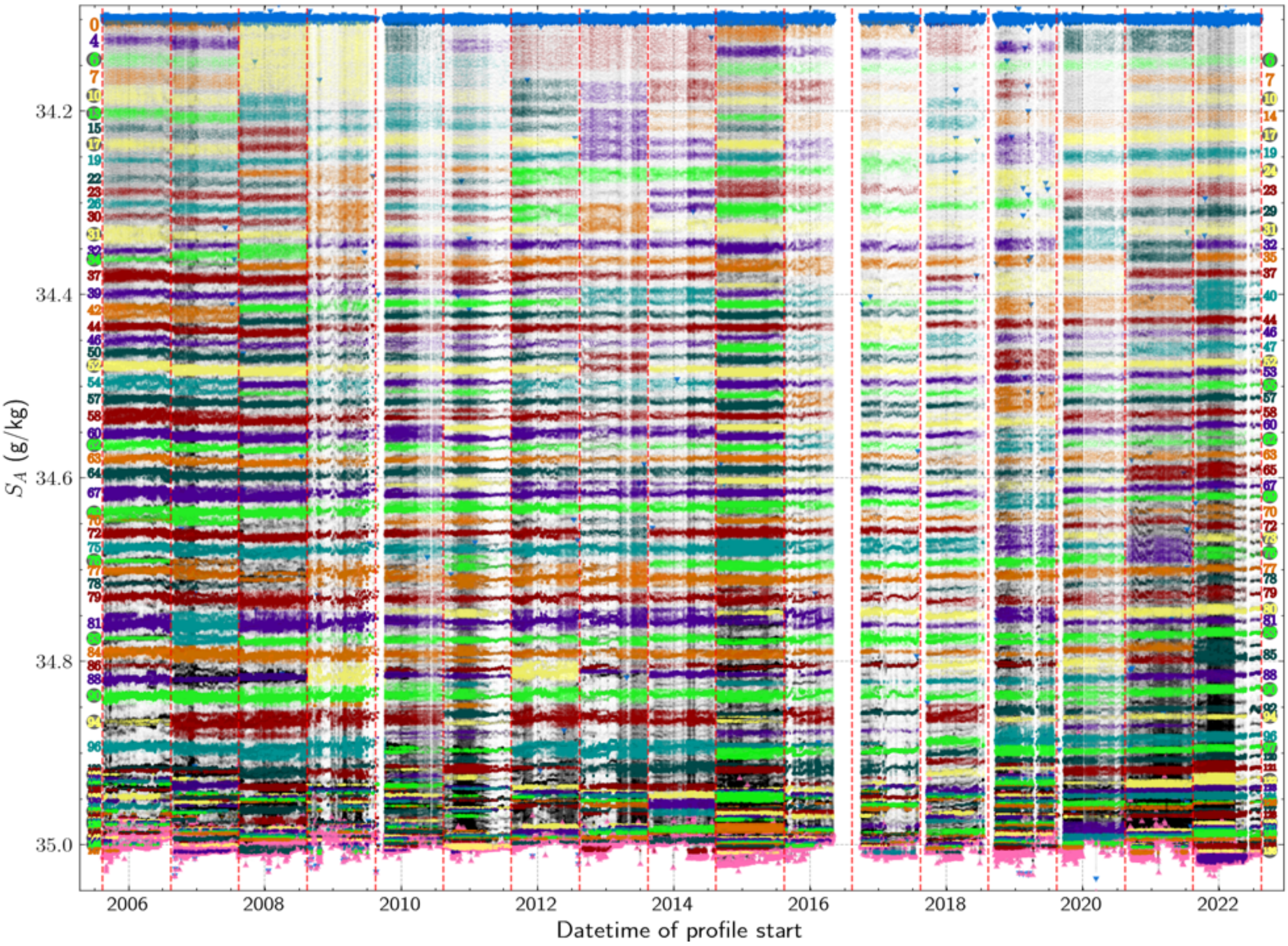

Figure S8. The same as Figure S7, with the cluster labels re-numbered to manually connect layers across the time periods, as described in Text S4.

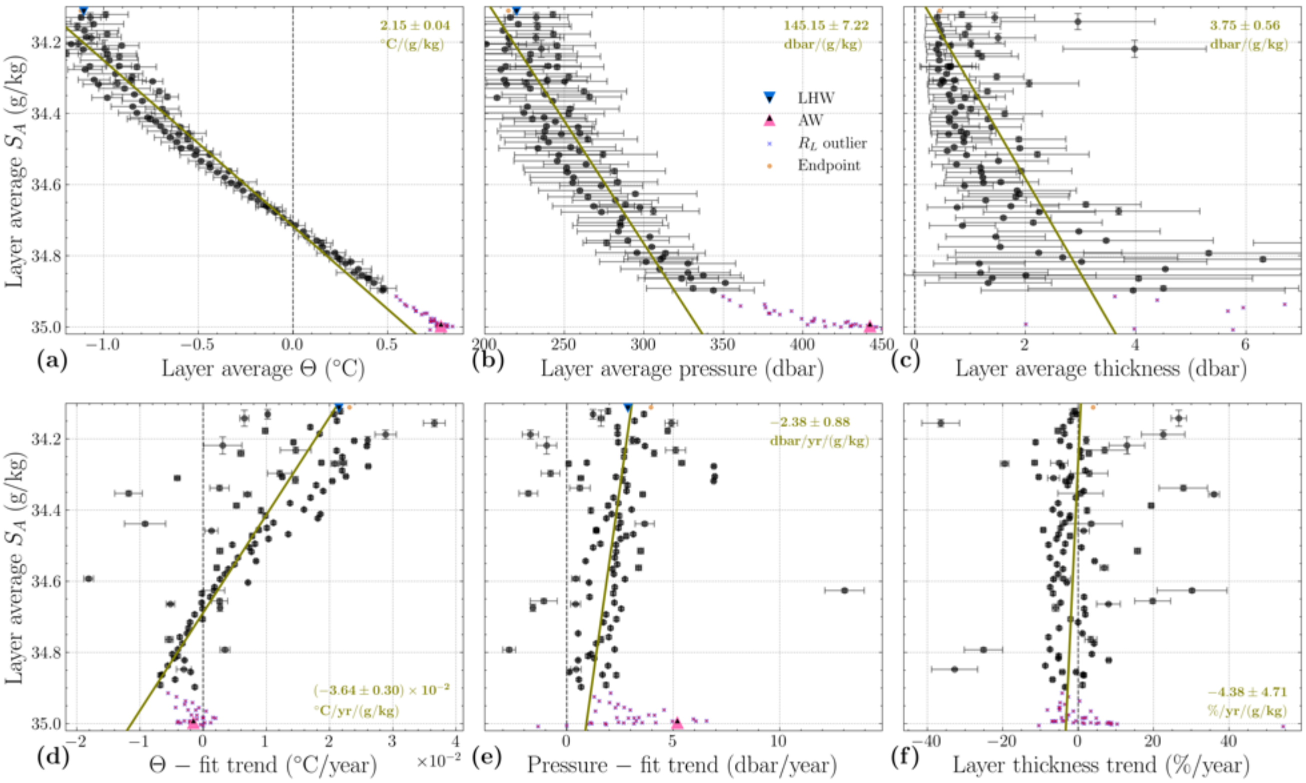

Figure S9. Averages and fit-corrected trends for all manually connected layers (see Text S4) as functions of layer average absolute salinity. In all panels, vertical error bars show the standard deviation in each layer's absolute salinity, however many are very small. The top row shows layer average (a) temperature, (b) pressure, and (c) thickness, with horizontal error bars representing the standard deviation for each layer in the respective variable. The bottom row shows the fit-corrected trends in (d) temperature, (e) pressure, and (f) thickness, with horizontal error bars representing the standard error on each layer's trend calculation. Layer thickness trends have been normalized to show percent changes. All outliers were ignored when calculating the fit lines.

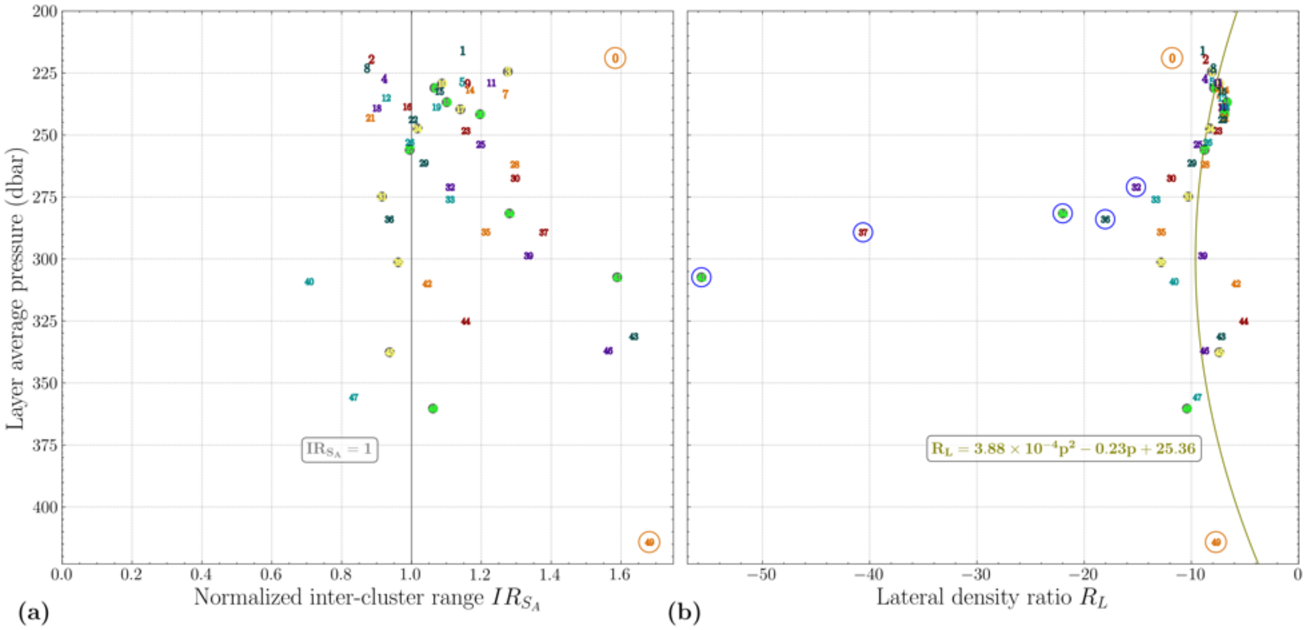

Figure S10. The value of each layer's (a) normalized inter-layer range for salinity IR_{S_A} and (b) lateral density ratio R_L as a function of the layer's average pressure. The colors for each layer are the same as in Figure 3 in the main text and the numbers correspond to the layers described in Table 3. Blue circles mark the outliers in R_L and orange circles denote endpoint clusters.

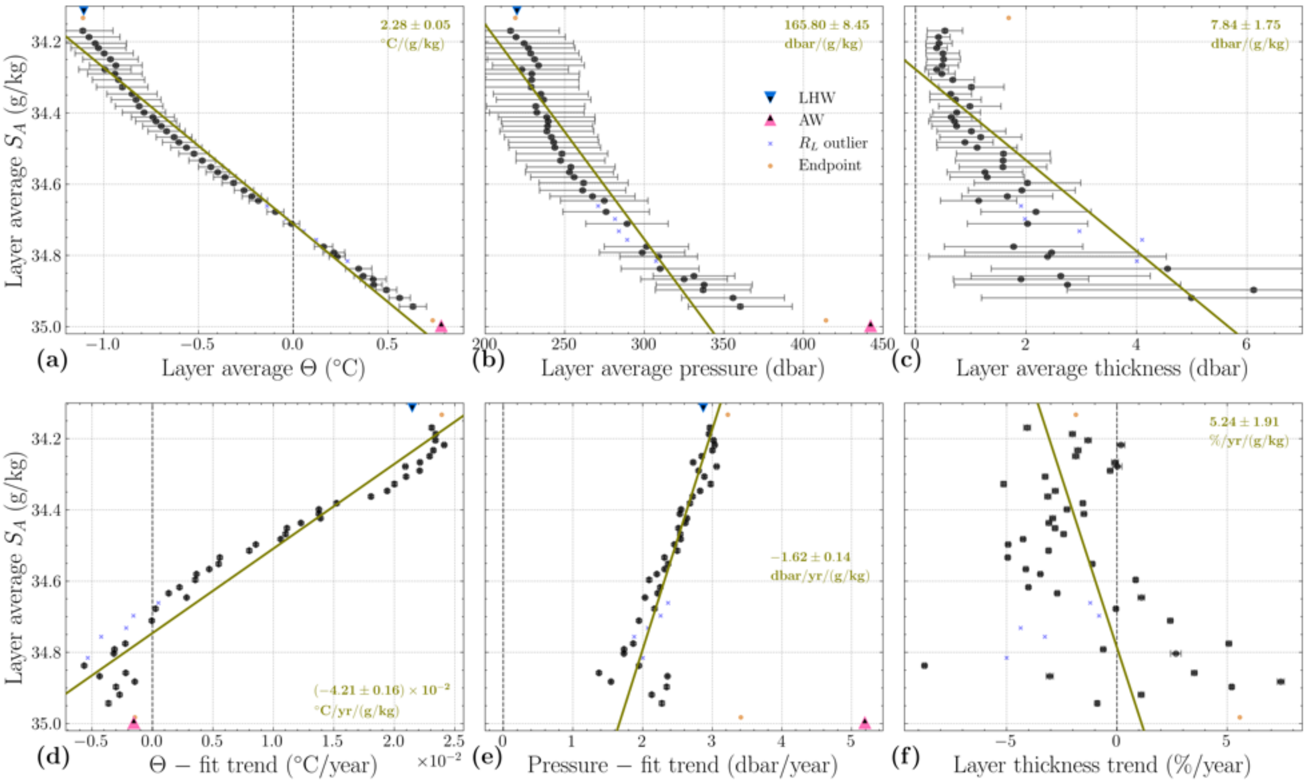

Figure S11. Averages and trends for all detected layers as functions of layer average salinity where outlier layers in R_L have been excluded from the linear fit lines. In all panels, vertical error bars show the standard deviation in each layer's salinity, but are too small to be seen. The top row shows layer average (a) temperature, (b) pressure, and (c) thickness, with horizontal error bars representing the standard deviation for each layer in the respective variable. The bottom row shows the trends in spatially corrected (d) temperature, (e) pressure, and (f) thickness, all with horizontal error bars representing the standard error of the estimated slope on each layer's trend calculation. Layer thickness trends in (f) have been normalized to show percent changes from average thicknesses in (c). The blue and pink triangle markers denote the values for the LHW and AW cores, respectively, blue markers denote outliers in R_L, and orange markers denote endpoint clusters.

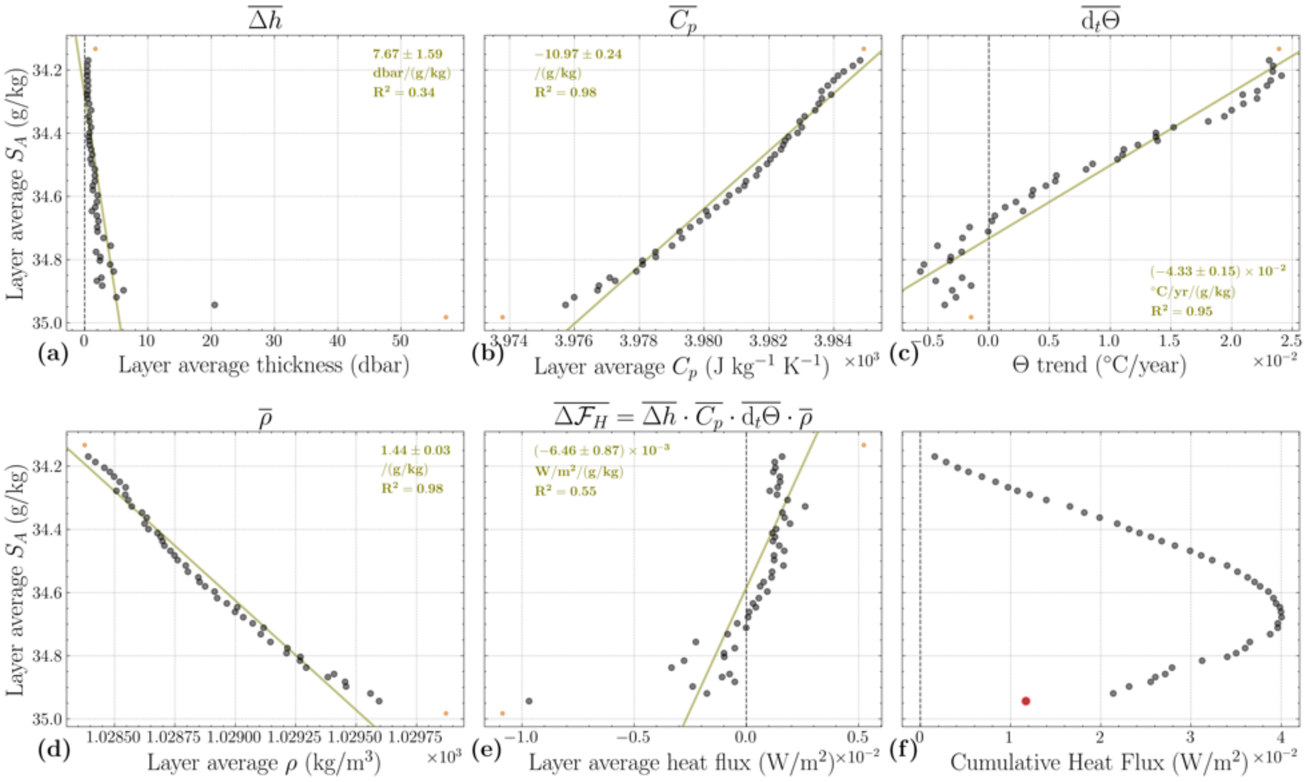

Figure S12. Plots of the various components of heat flux for each layer as a function of layer average salinity: The layer averages for (a) thickness (same as Figure 4c in the main text, with a wider horizontal domain), (b) isobaric heat capacity, (c) fit-corrected trend in temperature over time (same as Figure 4d in the main text), (d) density, (e) net heat flux, and (f) the cumulative net heat flux of regular layers, from the top to the bottom of the staircase. The red marker in (f) represents the layer which is an outlier in (e).

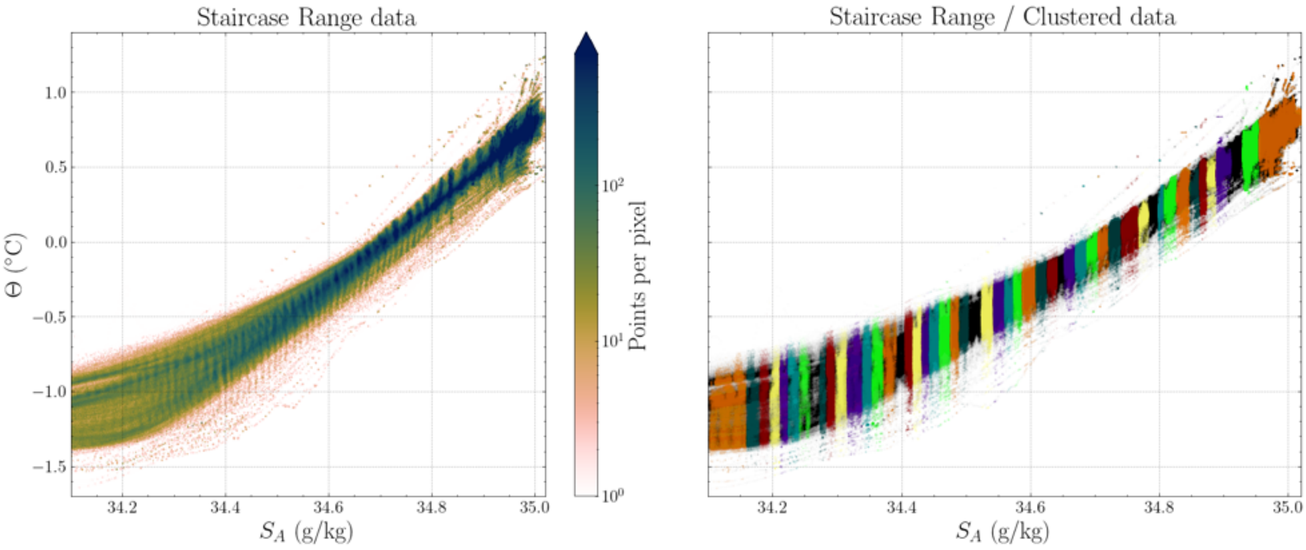

(a) (b)

Figure S13. (a) The density of observations in temperature-salinity space for *Staircase Range* data, the 15,202 profiles in the BGR for the date range of this study which extend past 400 dbar. (b) The same as panel a with the data points colored to distinguish the layers which were connected across the 17 year-long periods. Black points are those designated as noise by HDBSCAN.

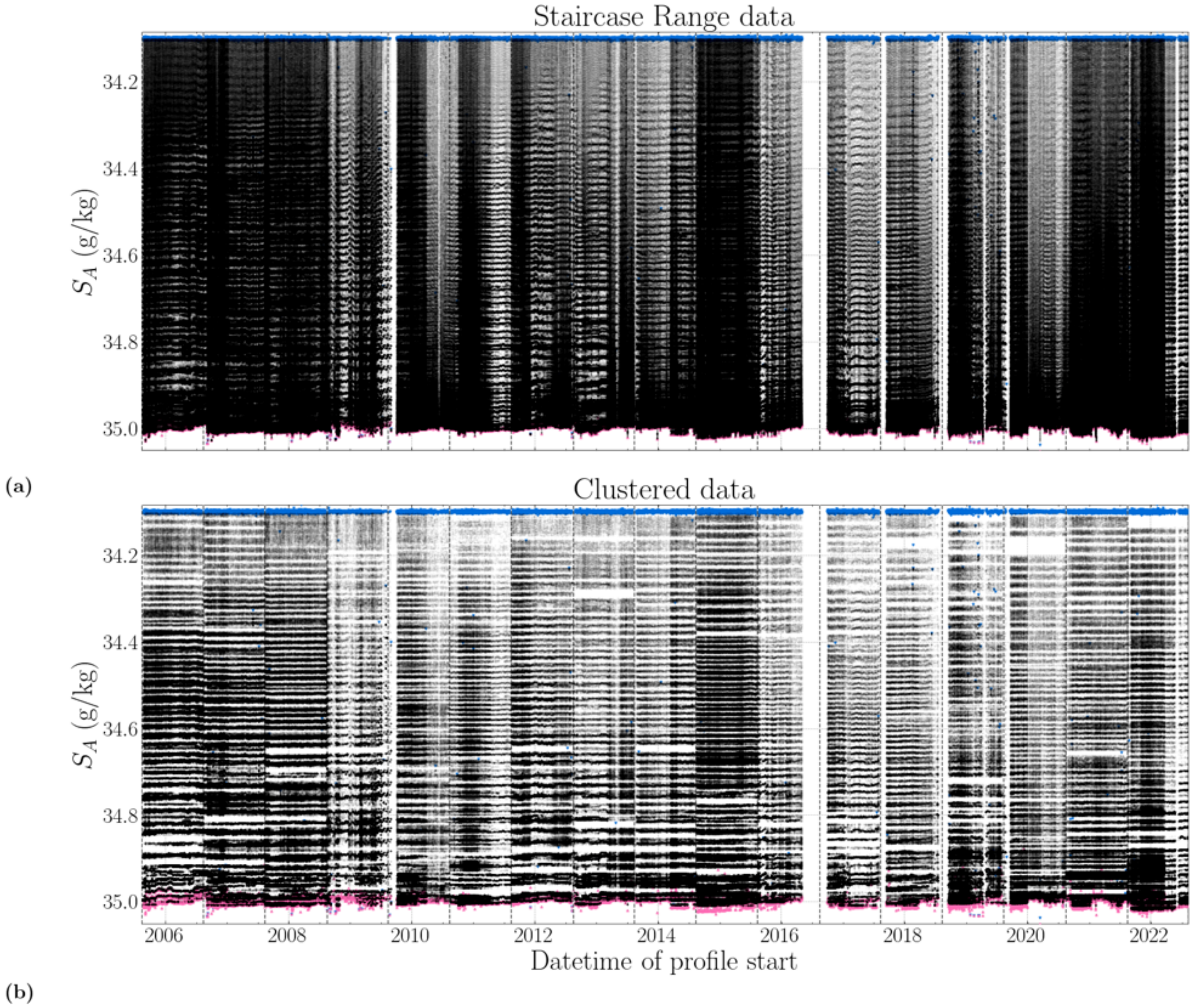

Figure S14. The salinity values of (a)*Staircase Range* and (b) *Clustered* data across time. The LHW and AW cores are marked in blue and pink, respectively. Panel (b) is the same plot as Figure 3a in the main text, but without points colored by detected layer.

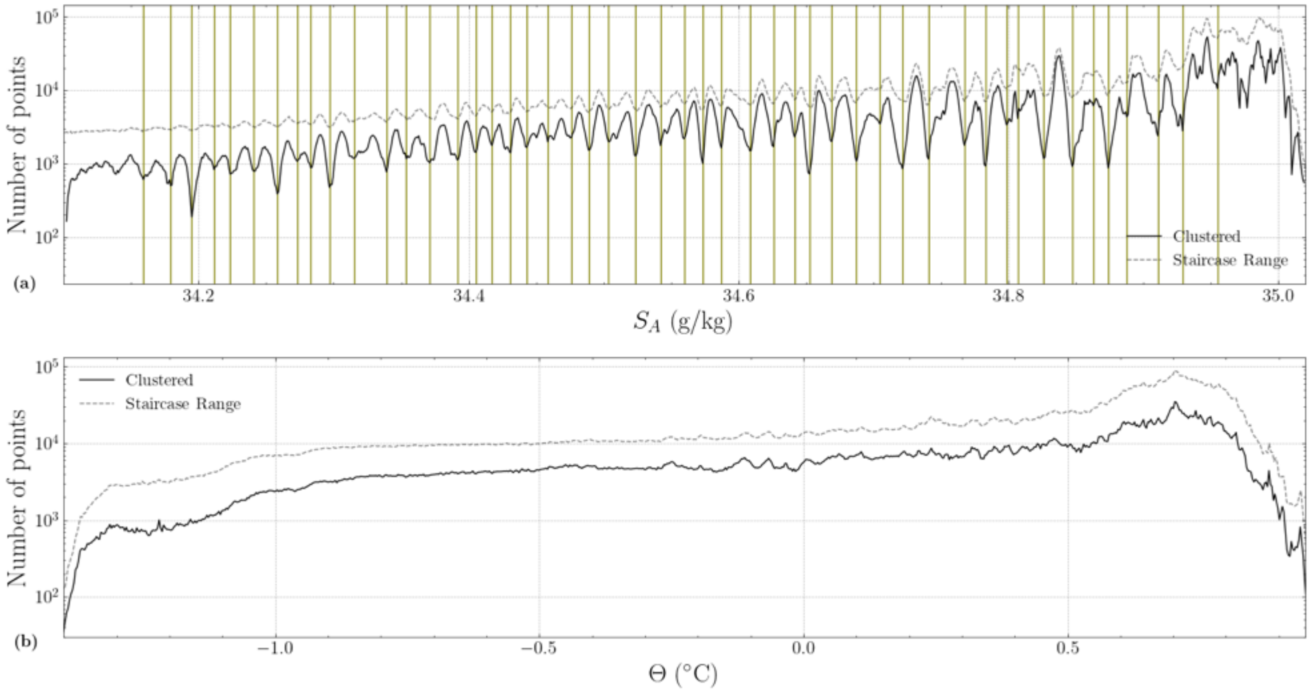

Figure S15. Histograms of (a) salinity and (b) temperature across the ranges used in this study. Dotted lines represent the histograms of all the *Staircase Range* data and solid lines represent the *Clustered* data. Vertical lines in (a) denote the boundaries between layers.

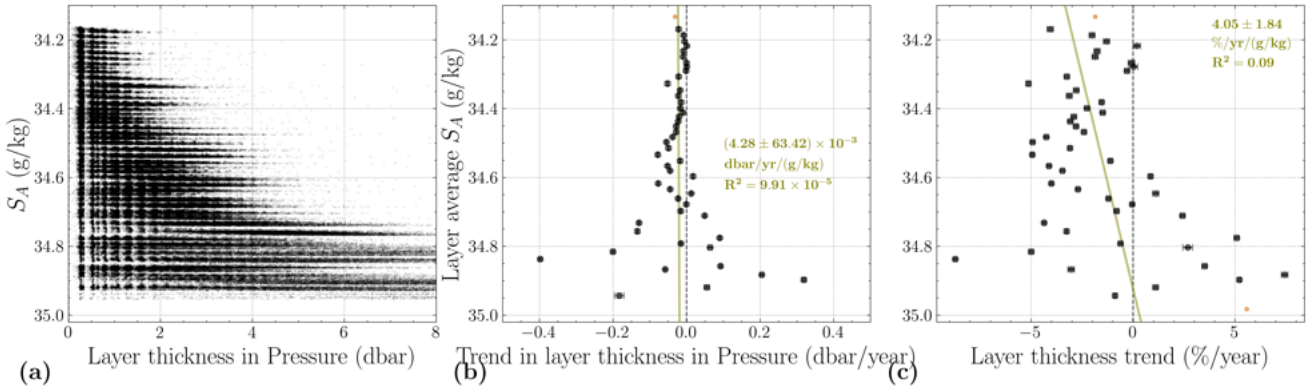

Figure S16. As functions of salinity, the (a) layer thicknesses for each profile, (b) layer thickness trends, and (c) percent change layer thickness trend. Panel (c) is the same as Figure 4f in the main text, reproduced here for comparison to panel (b).

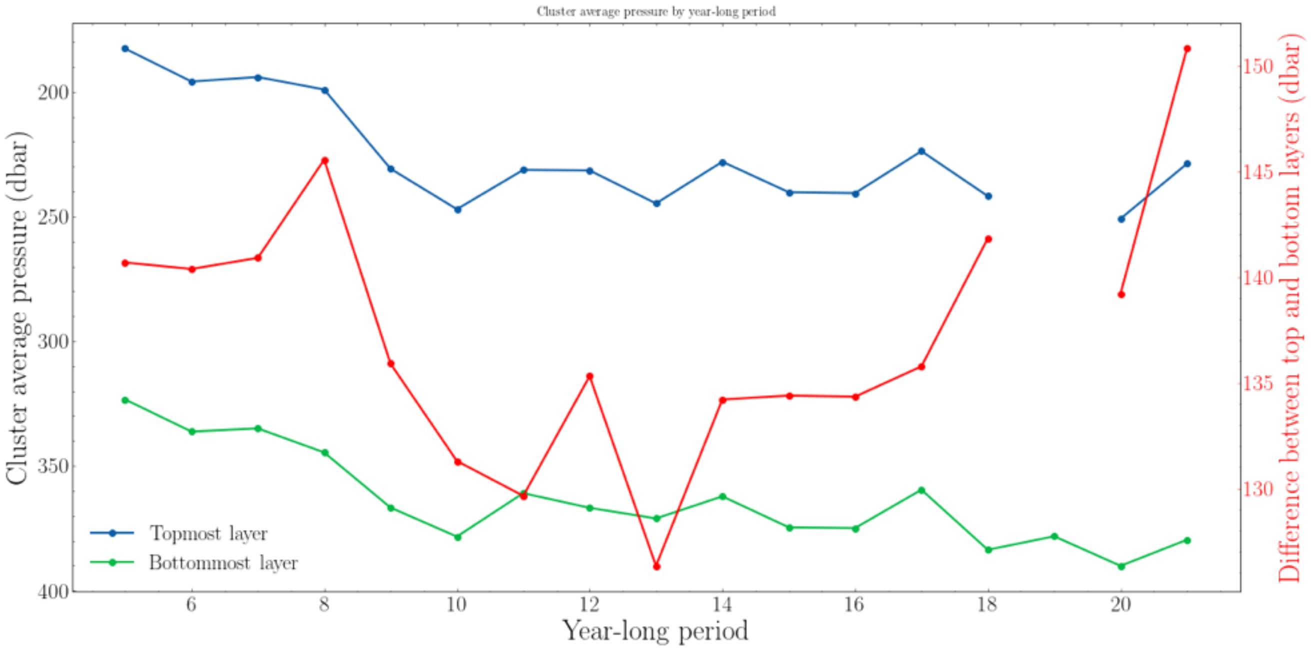

Figure S17. The layer-average pressure of the top and bottom detected staircases for each year-long period. The difference between the two is shown on the right-hand axis.

Table S1. For each year-long period, summaries of the data and clustering parameters used where $n_{clusters}$ is the number of clusters found in that period and $n^*_{clusters}$ is the number of those clusters in the salinity range $34.152 < S_A < 34.970$. Each time period is labeled by the last two digits of the year in which it began, i.e. 05 is the period from 15 August 2005 to 15 August 2006.

Time Period	ITPs present	Profiles used	Total points	Noise points	m_{pts}	$n_{clusters}$	DBCV	$n^*_{clusters}$
05	1, 3	1,425	1,152,866	616,986	650	75	0.2869	61
06	1, 3, 4, 5, 6, 8, 13	1,518	1,267,893	739,831	1100	68	0.2539	55
07	4, 5, 6, 8, 13, 18, 21, 30	1,454	1,126,688	623,000	1300	56	0.3172	50
08	8, 11, 18, 21, 25, 30	573	509,054	509,054	450	65	0.1615	52
09	21, 32, 33, 34, 35	774	628,730	400,559	300	80	0.1797	63
10	33, 41, 42, 43	743	621,887	446,750	500	78	0.1193	65
11	41, 52, 53, 54, 55	880	709,249	406,165	1300	54	0.2632	48
12	41, 62, 64, 65	597	473,227	278,529	1100	49	0.2256	42
13	64, 68, 69, 70, 77, 78, 79, 80	611	493,043	228,962	1350	47	0.2910	43
14	77, 79, 80, 81, 82, 84, 85, 86, 87	1,907	1,600,412	947,319	1050	79	0.2537	64
15	82, 85, 86, 88, 89	377	290,354	170,627	500	64	0.1772	52
16	97, 99	397	318,621	194,903	200	82	0.2130	64
17	97, 100, 101, 108	470	344,856	190,093	550	67	0.1973	55
18	103, 104, 105, 107, 109, 110	684	615,743	410,198	700	68	0.1433	55
19	105, 113, 114, 117, 118	488	443,676	268,088	750	61	0.1791	56
20	113, 114, 120, 121	1,063	967,756	707,763	1150	68	0.1719	55
21	120, 121, 122, 123	1,241	1,180,791	722,087	1150	63	0.1823	54
Average	5 ITPs	894	749,697	462,407	829	66	0.2127	55
Stdev	2 ITPs	459	390,147	231,635	378	11	0.0565	7
Total	60 different ITPs	15,202	12,744,846	7,860,914	–	–	–	–

Table S2. Summary of averages and standard deviations for each variable v for σ_v, the standard deviation of a layer in v; Δv, the distance between the average values in v for neighboring layers; and v_{span}, the distance between $v_{\max}$ and $v_{\min}$ for a layer.

Variable	Temperature (Θ)	Pressure (p)	Salinity (S_A)
$\overline{\sigma_v}$	$(8.88 \pm 4.07) \times 10^{-2}$ °C	28.6 ± 1.9 dbar	$(3.93 \pm 0.92) \times 10^{-3}$ g kg^{-1}
$\overline{\Delta v}$	$(3.95 \pm 1.63) \times 10^{-2}$ °C	4.73 ± 4.53 dbar	$(1.65 \pm 0.34) \times 10^{-2}$ g kg^{-1}
$\overline{v_{\mathrm{span}}}$	0.890 ± 0.107 °C	218 ± 25 dbar	$(1.66 \pm 0.39) \times 10^{-2}$ g kg^{-1}

Table S3. Slopes, intercepts, and R^2 values for the linear fits shown in each panel of Figure 4.

Linear fit with layer average salinity	Slope	Units	Intercept	R^2
Layer average Θ	2.29 ± 0.04	°C g kg^{-1}	-79.36 ± 1.43	0.99
Layer average pressure	162.5 ± 7.9	dbar g kg^{-1}	-5348 ± 273	0.90
Layer average thickness	7.67 ± 1.59	dbar g kg^{-1}	-262.9 ± 54.9	0.34
Θ trend	-0.0433 ± 0.0015	°C yr^{-1} g kg $^{-1}$	1.50 ± 0.05	0.95
Pressure trend	-1.62 ± 0.13	dbar yr^{-1} g kg^{-1}	58.3 ± 4.4	0.78
Layer thickness trend	4.05 ± 1.84	% yr^{-1} g kg^{-1}	-141.6 ± 63.7	0.09

Table S4. For each detected layer, the values of the lateral density ratio R_L, inter-cluster range in salinity IR_{S_A}, and salinity boundary; the average values of salinity S_A, temperature Θ, pressure p, and thickness Δp; as well as the trends in time for salinity S_A, temperature Θ, pressure p, and thickness Δp and their corresponding R^2 values. Endpoint layers are marked in orange text and outlier layers in R_L are marked in blue text.

Table 1: For each detected layer, the values of the lateral density ratio R_L, inter-cluster range in salinity IR_{S_A}, and salinity division; the average values of salinity S_A, temperature Θ, pressure p, and thickness Δp; as well as the trends in time for salinity S_A, temperature Θ, pressure p, and thickness Δp and their corresponding R^2 values. Endpoint layers are marked in orange text and outlier layers in R_L are marked in blue text.

	Divisions			Layer averages				Trends across time									
ID	R_L	IR_{S_A}	$S_{A,\text{ min}}$	$\overline{S_A}$ (g/kg)	$\overline{\Theta}$ (°C)	$\overline{p}$ (dbar)	$\overline{\Delta p}$ (dbar)	$d\overline{\Theta}/dt$(°C/yr)	R^2	$d\overline{\Theta_{fit}}/dt$ (°C/yr)	R^2	$d\overline{p}/dt$ (dbar/yr)	R^2	$d\overline{p_{fit}}/dt$ (dbar/yr)	R^2	$d\overline{\Delta p}/dt$ (dbar/yr)	R^2
0	−11.8	1.6	34.100	34.133 ± 0.015	−1.11 ± 0.15	218.94 ± 30.49	1.68 ± 0.90	$(2.631\pm0.006)\times10^{-2}$	0.80	$(2.391\pm0.006)\times10^{-2}$	0.77	3.96 ± 0.02	0.43	3.22 ± 0.01	0.65	$(-3.14\pm0.17)\times10^{-2}$	0.03
1	−9.0	1.1	34.159	34.1690 ± 0.0053	−1.11 ± 0.16	215.91 ± 30.65	0.53 ± 0.32	$(2.733\pm0.010)\times10^{-2}$	0.82	$(2.31\pm0.01)\times10^{-2}$	0.75	3.81 ± 0.03	0.43	2.96 ± 0.02	0.60	$(-2.16\pm0.08)\times10^{-2}$	0.13
2	−8.7	0.9	34.179	34.1866 ± 0.0037	−1.08 ± 0.16	219.38 ± 30.98	0.41 ± 0.21	$(2.728\pm0.010)\times10^{-2}$	0.84	$(2.34\pm0.01)\times10^{-2}$	0.77	3.70 ± 0.03	0.43	2.95 ± 0.02	0.61	$(-8.36\pm0.56)\times10^{-3}$	0.05
3	−8.1	1.3	34.195	34.2045 ± 0.0040	−1.05 ± 0.17	224.39 ± 31.15	0.42 ± 0.24	$(2.64\pm0.01)\times10^{-2}$	0.76	$(2.34\pm0.01)\times10^{-2}$	0.71	3.47 ± 0.04	0.37	3.02 ± 0.02	0.62	$(-5.56\pm0.61)\times10^{-3}$	0.02
4	−8.7	0.9	34.211	34.2175 ± 0.0032	−1.03 ± 0.15	227.18 ± 29.31	0.38 ± 0.19	$(2.68\pm0.01)\times10^{-2}$	0.75	$(2.41\pm0.01)\times10^{-2}$	0.73	3.60 ± 0.04	0.33	3.03 ± 0.02	0.57	$(7.02\pm6.96)\times10^{-4}$	2.55×10^{-4}
5	−8.1	1.1	34.223	34.2327 ± 0.0045	−1.00 ± 0.15	228.55 ± 30.37	0.49 ± 0.30	$(2.56\pm0.01)\times10^{-2}$	0.74	$(2.322\pm0.010)\times10^{-2}$	0.72	3.43 ± 0.03	0.34	3.00 ± 0.02	0.59	$(-8.73\pm0.71)\times10^{-3}$	0.02
6	−7.9	1.1	34.241	34.2491 ± 0.0042	−0.96 ± 0.15	230.98 ± 29.58	0.51 ± 0.30	$(2.474\pm0.010)\times10^{-2}$	0.76	$(2.292\pm0.009)\times10^{-2}$	0.75	3.13 ± 0.03	0.30	2.85 ± 0.02	0.58	$(-9.44\pm0.74)\times10^{-3}$	0.02
7	−7.5	1.3	34.258	34.2663 ± 0.0035	−0.94 ± 0.14	233.48 ± 28.83	0.48 ± 0.29	$(2.40\pm0.01)\times10^{-2}$	0.73	$(2.212\pm0.009)\times10^{-2}$	0.72	3.05 ± 0.03	0.27	2.73 ± 0.02	0.55	$(-4.09\pm7.62)\times10^{-4}$	4.53×10^{-5}
8	−8.0	0.9	34.273	34.2779 ± 0.0027	−0.99 ± 0.14	223.05 ± 29.26	0.38 ± 0.21	$(2.36\pm0.01)\times10^{-2}$	0.66	$(2.09\pm0.01)\times10^{-2}$	0.62	3.19 ± 0.05	0.26	3.06 ± 0.03	0.52	$(6.72\pm81.15)\times10^{-5}$	1.92×10^{-6}
9	−7.5	1.2	34.283	34.2898 ± 0.0032	−0.94 ± 0.14	229.26 ± 30.00	0.47 ± 0.24	$(2.468\pm0.008)\times10^{-2}$	0.79	$(2.209\pm0.008)\times10^{-2}$	0.77	3.37 ± 0.03	0.34	2.80 ± 0.02	0.58	$(-1.45\pm0.54)\times10^{-3}$	9.69×10^{-4}
10	−7.4	1.1	34.297	34.3067 ± 0.0042	−0.92 ± 0.14	229.17 ± 29.73	0.67 ± 0.39	$(2.356\pm0.008)\times10^{-2}$	0.73	$(2.097\pm0.008)\times10^{-2}$	0.71	3.42 ± 0.03	0.33	2.89 ± 0.01	0.55	$(-2.19\pm0.08)\times10^{-2}$	0.08
11	−7.6	1.2	34.315	34.3272 ± 0.0062	−0.90 ± 0.14	228.88 ± 30.00	1.01 ± 0.59	$(2.267\pm0.007)\times10^{-2}$	0.71	$(2.000\pm0.007)\times10^{-2}$	0.68	3.52 ± 0.02	0.35	2.98 ± 0.01	0.56	$(-5.18\pm0.10)\times10^{-2}$	0.19
12	−7.2	0.9	34.339	34.3466 ± 0.0036	−0.85 ± 0.13	234.93 ± 29.81	0.64 ± 0.38	$(2.256\pm0.009)\times10^{-2}$	0.66	$(1.941\pm0.008)\times10^{-2}$	0.64	3.55 ± 0.03	0.33	2.83 ± 0.02	0.51	$(-1.78\pm0.08)\times10^{-2}$	0.05
13	−6.7	1.1	34.354	34.3625 ± 0.0045	−0.83 ± 0.13	236.70 ± 29.67	0.72 ± 0.47	$(2.090\pm0.009)\times10^{-2}$	0.62	$(1.807\pm0.008)\times10^{-2}$	0.63	3.31 ± 0.03	0.31	2.72 ± 0.02	0.49	$(-2.27\pm0.10)\times10^{-2}$	0.06
14	−6.9	1.2	34.371	34.3813 ± 0.0048	−0.81 ± 0.13	231.78 ± 30.83	0.98 ± 0.56	$(1.882\pm0.006)\times10^{-2}$	0.68	$(1.523\pm0.006)\times10^{-2}$	0.62	3.51 ± 0.02	0.40	2.68 ± 0.01	0.52	$(-1.52\pm0.10)\times10^{-2}$	0.02
15	−7.2	1.1	34.392	34.3986 ± 0.0033	−0.79 ± 0.11	232.43 ± 29.70	0.74 ± 0.43	$(1.757\pm0.007)\times10^{-2}$	0.65	$(1.376\pm0.006)\times10^{-2}$	0.59	3.66 ± 0.02	0.41	2.55 ± 0.01	0.47	$(-1.68\pm0.08)\times10^{-2}$	0.04
16	−7.1	1.0	34.405	34.4114 ± 0.0031	−0.74 ± 0.11	238.62 ± 30.39	0.65 ± 0.37	$(1.661\pm0.007)\times10^{-2}$	0.61	$(1.376\pm0.006)\times10^{-2}$	0.59	3.35 ± 0.03	0.35	2.53 ± 0.01	0.49	$(-9.66\pm0.74)\times10^{-3}$	0.02
17	−6.9	1.1	34.417	34.4235 ± 0.0036	−0.72 ± 0.11	239.58 ± 29.41	0.70 ± 0.47	$(1.627\pm0.008)\times10^{-2}$	0.57	$(1.390\pm0.007)\times10^{-2}$	0.56	3.19 ± 0.03	0.30	2.64 ± 0.02	0.47	$(-2.05\pm0.09)\times10^{-2}$	0.05
18	−7.1	0.9	34.431	34.4367 ± 0.0030	−0.70 ± 0.10	239.17 ± 28.46	0.74 ± 0.45	$(1.449\pm0.007)\times10^{-2}$	0.52	$(1.227\pm0.006)\times10^{-2}$	0.52	3.33 ± 0.03	0.32	2.61 ± 0.01	0.46	$(-2.29\pm0.09)\times10^{-2}$	0.06
19	−6.9	1.1	34.443	34.4513 ± 0.0043	−0.67 ± 0.10	238.70 ± 29.55	1.01 ± 0.62	$(1.365\pm0.006)\times10^{-2}$	0.54	$(1.112\pm0.005)\times10^{-2}$	0.54	3.38 ± 0.02	0.37	2.51 ± 0.01	0.48	$(-2.83\pm0.11)\times10^{-2}$	0.06
20	−6.9	1.2	34.459	34.4676 ± 0.0046	−0.63 ± 0.09	241.56 ± 29.43	1.18 ± 0.74	$(1.341\pm0.005)\times10^{-2}$	0.55	$(1.101\pm0.005)\times10^{-2}$	0.52	3.52 ± 0.02	0.39	2.54 ± 0.01	0.48	$(-2.85\pm0.13)\times10^{-2}$	0.04
21	−6.9	0.9	34.476	34.4822 ± 0.0032	−0.60 ± 0.09	243.04 ± 28.30	0.89 ± 0.51	$(1.247\pm0.006)\times10^{-2}$	0.51	$(1.059\pm0.005)\times10^{-2}$	0.53	3.38 ± 0.02	0.36	2.55 ± 0.01	0.47	$(-3.80\pm0.09)\times10^{-2}$	0.14
22	−7.1	1.0	34.489	34.4968 ± 0.0034	−0.56 ± 0.08	243.73 ± 28.85	1.11 ± 0.73	$(1.088\pm0.005)\times10^{-2}$	0.48	$(8.55\pm0.04)\times10^{-3}$	0.46	3.60 ± 0.02	0.42	2.45 ± 0.01	0.47	$(-5.50\pm0.11)\times10^{-2}$	0.16
23	−7.6	1.2	34.504	34.5143 ± 0.0051	−0.52 ± 0.08	248.24 ± 28.78	1.59 ± 0.85	$(9.84\pm0.05)\times10^{-3}$	0.41	$(8.00\pm0.04)\times10^{-3}$	0.41	3.28 ± 0.02	0.35	2.50 ± 0.01	0.47	$(-4.93\pm0.14)\times10^{-2}$	0.09
24	−8.3	1.0	34.524	34.5336 ± 0.0043	−0.48 ± 0.07	247.33 ± 27.97	1.58 ± 0.86	$(7.38\pm0.04)\times10^{-3}$	0.29	$(5.57\pm0.03)\times10^{-3}$	0.27	3.48 ± 0.02	0.40	2.314 ± 0.009	0.43	$(-7.84\pm0.13)\times10^{-2}$	0.23
25	−9.4	1.2	34.542	34.5517 ± 0.0045	−0.43 ± 0.06	253.79 ± 27.88	1.58 ± 0.79	$(6.23\pm0.05)\times10^{-3}$	0.21	$(5.47\pm0.04)\times10^{-3}$	0.25	3.30 ± 0.02	0.32	2.37 ± 0.01	0.41	$(-1.77\pm0.14)\times10^{-2}$	0.01
26	−8.5	1.0	34.560	34.5662 ± 0.0031	−0.40 ± 0.06	252.97 ± 27.65	1.26 ± 0.68	$(5.79\pm0.05)\times10^{-3}$	0.21	$(4.69\pm0.04)\times10^{-3}$	0.22	3.56 ± 0.02	0.39	2.32 ± 0.01	0.42	$(-5.18\pm0.12)\times10^{-2}$	0.14
27	−8.8	1.0	34.573	34.5801 ± 0.0031	−0.36 ± 0.06	255.92 ± 27.33	1.30 ± 0.67	$(4.77\pm0.04)\times10^{-3}$	0.15	$(3.64\pm0.03)\times10^{-3}$	0.15	3.55 ± 0.02	0.40	2.20 ± 0.01	0.40	$(-4.50\pm0.11)\times10^{-2}$	0.11
28	−8.8	1.3	34.587	34.5964 ± 0.0053	−0.31 ± 0.06	261.85 ± 27.95	2.03 ± 0.96	$(4.53\pm0.04)\times10^{-3}$	0.14	$(3.54\pm0.03)\times10^{-3}$	0.14	3.15 ± 0.02	0.33	2.093 ± 0.009	0.38	$(1.72\pm0.16)\times10^{-2}$	0.01
29	−10.0	1.0	34.608	34.6172 ± 0.0038	−0.26 ± 0.05	261.26 ± 27.08	1.92 ± 0.97	$(3.19\pm0.03)\times10^{-3}$	0.09	$(2.23\pm0.03)\times10^{-3}$	0.07	3.67 ± 0.01	0.43	2.253 ± 0.009	0.40	$(-7.72\pm0.15)\times10^{-2}$	0.16
30	−11.9	1.3	34.626	34.6341 ± 0.0038	−0.22 ± 0.05	267.42 ± 26.74	1.66 ± 0.82	$(2.33\pm0.04)\times10^{-3}$	0.04	$(1.34\pm0.03)\times10^{-3}$	0.02	3.45 ± 0.02	0.33	2.22 ± 0.01	0.34	$(-4.49\pm0.15)\times10^{-2}$	0.07
31	−10.3	0.9	34.641	34.6461 ± 0.0025	−0.18 ± 0.05	274.80 ± 27.45	1.14 ± 0.69	$(3.22\pm0.05)\times10^{-3}$	0.10	$(2.82\pm0.05)\times10^{-3}$	0.10	2.44 ± 0.03	0.17	2.03 ± 0.02	0.34	$(1.26\pm0.17)\times10^{-2}$	0.01
32	−15.2	1.1	34.653	34.6610 ± 0.0034	−0.14 ± 0.04	270.99 ± 26.97	1.91 ± 0.90	$(3.60\pm0.32)\times10^{-4}$	0.00	$(4.91\pm0.27)\times10^{-4}$	0.00	3.81 ± 0.02	0.41	2.364 ± 0.010	0.40	$(-2.31\pm0.17)\times10^{-2}$	0.01
33	−13.3	1.1	34.669	34.6776 ± 0.0040	−0.09 ± 0.04	275.96 ± 27.17	2.18 ± 1.00	$(2.20\pm0.29)\times10^{-4}$	5.42×10^{-4}	$(2.46\pm0.25)\times10^{-4}$	9.10×10^{-4}	3.51 ± 0.01	0.37	2.170 ± 0.009	0.37	$(-1.02\pm1.76)\times10^{-3}$	2.54×10^{-5}
34	−22.0	1.3	34.687	34.6973 ± 0.0044	−0.04 ± 0.05	281.59 ± 28.33	1.98 ± 1.11	$(-2.12\pm0.03)\times10^{-3}$	0.05	$(-1.58\pm0.03)\times10^{-3}$	0.04	2.99 ± 0.02	0.31	2.258 ± 0.010	0.46	$(-1.61\pm0.21)\times10^{-2}$	0.01
35	−12.8	1.2	34.705	34.7110 ± 0.0036	−0.009 ± 0.042	289.12 ± 25.85	2.03 ± 1.09	$(-6.43\pm3.93)\times10^{-5}$	3.70×10^{-5}	$(-5.76\pm3.60)\times10^{-5}$	3.54×10^{-5}	2.26 ± 0.02	0.13	1.95 ± 0.01	0.29	$(4.91\pm0.22)\times10^{-2}$	0.04
36	−18.0	0.9	34.721	34.7316 ± 0.0036	0.05 ± 0.05	283.96 ± 25.88	2.97 ± 1.43	$(-2.71\pm0.03)\times10^{-3}$	0.07	$(-2.18\pm0.02)\times10^{-3}$	0.06	3.57 ± 0.01	0.38	2.075 ± 0.008	0.32	−0.13±0.00	0.21
37	−40.6	1.4	34.741	34.7561 ± 0.0060	0.12 ± 0.05	289.24 ± 25.62	4.10 ± 1.73	$(-5.18\pm0.02)\times10^{-3}$	0.21	$(-4.24\pm0.02)\times10^{-3}$	0.18	3.03 ± 0.01	0.33	1.879 ± 0.007	0.30	−0.13±0.00	0.17
38	−12.8	1.0	34.767	34.7754 ± 0.0036	0.16 ± 0.05	301.33 ± 26.48	1.77 ± 1.25	$(-2.18\pm0.03)\times10^{-3}$	0.06	$(-2.24\pm0.03)\times10^{-3}$	0.07	2.03 ± 0.02	0.16	1.87 ± 0.01	0.34	$(9.01\pm0.21)\times10^{-2}$	0.15
39	−9.0	1.3	34.783	34.7916 ± 0.0034	0.22 ± 0.06	298.68 ± 26.82	2.46 ± 1.57	$(-4.13\pm0.03)\times10^{-3}$	0.17	$(-3.14\pm0.02)\times10^{-3}$	0.14	2.86 ± 0.01	0.38	1.733 ± 0.007	0.36	$(-1.53\pm0.26)\times10^{-2}$	0.00
40	−11.6	0.7	34.799	34.8033 ± 0.0022	0.23 ± 0.04	309.02 ± 24.38	2.39 ± 2.15	$(-3.40\pm0.04)\times10^{-3}$	0.12	$(-3.19\pm0.04)\times10^{-3}$	0.11	1.38 ± 0.03	0.06	1.73 ± 0.01	0.28	$(6.40\pm0.57)\times10^{-2}$	0.02
41	−55.7	1.6	34.807	34.8155 ± 0.0045	0.29 ± 0.06	307.35 ± 27.50	4.00 ± 2.70	$(-6.97\pm0.03)\times10^{-3}$	0.29	$(-5.35\pm0.03)\times10^{-3}$	0.21	3.66 ± 0.01	0.38	2.002 ± 0.008	0.30	−0.20±0.00	0.16
42	−5.9	1.0	34.826	34.8372 ± 0.0035	0.35 ± 0.07	309.87 ± 24.48	4.56 ± 3.19	$(-6.51\pm0.03)\times10^{-3}$	0.19	$(-5.65\pm0.02)\times10^{-3}$	0.26	3.217 ± 0.008	0.38	1.947 ± 0.006	0.33	−0.40±0.00	0.43
43	−7.3	1.6	34.847	34.8575 ± 0.0038	0.37 ± 0.05	331.20 ± 25.64	2.63 ± 1.62	$(-1.85\pm0.04)\times10^{-3}$	0.03	$(-2.21\pm0.03)\times10^{-3}$	0.07	1.63 ± 0.02	0.09	1.37 ± 0.01	0.20	$(9.21\pm0.32)\times10^{-2}$	0.08
44	−5.1	1.2	34.863	34.8670 ± 0.0026	0.42 ± 0.07	325.00 ± 27.15	1.91 ± 1.23	$(-5.05\pm0.06)\times10^{-3}$	0.10	$(-4.38\pm0.04)\times10^{-3}$	0.17	3.66 ± 0.02	0.32	2.36 ± 0.01	0.33	$(-5.81\pm0.30)\times10^{-2}$	0.05
45	−7.4	0.9	34.874	34.8823 ± 0.0032	0.43 ± 0.04	337.59 ± 30.16	2.75 ± 2.05	$(-1.55\pm0.04)\times10^{-3}$	0.02	$(-1.46\pm0.03)\times10^{-3}$	0.03	0.74 ± 0.03	0.01	1.55 ± 0.01	0.22	0.20±0.00	0.25
46	−8.8	1.6	34.888	34.8970 ± 0.0051	0.49 ± 0.06	336.92 ± 29.91	6.12 ± 3.38	$(-3.61\pm0.02)\times10^{-3}$	0.11	$(-3.01\pm0.02)\times10^{-3}$	0.11	3.52 ± 0.01	0.34	2.345 ± 0.006	0.38	0.32±0.00	0.25
47	−9.5	0.8	34.911	34.9190 ± 0.0042	0.56 ± 0.06	355.69 ± 32.31	4.99 ± 3.80	$(-3.18\pm0.02)\times10^{-3}$	0.11	$(-2.72\pm0.02)\times10^{-3}$	0.13	3.06 ± 0.01	0.30	2.131 ± 0.008	0.34	$(5.50\pm0.65)\times10^{-2}$	0.01
48	−10.4	1.1	34.929	34.9432 ± 0.0062	0.63 ± 0.07	360.28 ± 32.66	20.54 ± 8.39	$(-5.74\pm0.02)\times10^{-3}$	0.18	$(-3.64\pm0.01)\times10^{-3}$	0.15	3.490 ± 0.007	0.32	2.276 ± 0.004	0.37	−0.18±0.01	0.01
49	−7.7	1.7	34.955	34.982 ± 0.015	0.74 ± 0.07	414.14 ± 39.93	57.08 ± 29.76	$(-2.11\pm0.01)\times10^{-3}$	0.02	$(-1.468\pm0.010)\times10^{-3}$	0.02	3.052 ± 0.006	0.16	3.411 ± 0.005	0.26	3.18±0.04	0.32